



A “Trap-Release-Amplify” Model of Chorus Waves

Xin Tao^{1,2,3} , Fulvio Zonca^{4,5} , and Liu Chen^{5,6}

Key Points:

- We propose a new model to explain frequency chirping of chorus as selective amplification of new emissions by phase-locking
- The model unifies two different estimates of chorus chirping rate from seemingly unrelated studies
- Fine structures of chorus and their dynamic evolution are explained by nonlinear electron phase space dynamics

Correspondence to:

X. Tao,
xtao@ustc.edu.cn

Citation:

Tao, X., Zonca, F., & Chen, L. (2021). A “Trap-Release-Amplify” model of chorus waves. *Journal of Geophysical Research: Space Physics*, 126, e2021JA029585. <https://doi.org/10.1029/2021JA029585>

Received 21 MAY 2021

Accepted 3 AUG 2021

¹CAS Key Laboratory of Geospace Environment, Department of Geophysics and Planetary Sciences, University of Science and Technology of China, Hefei, China, ²CAS Center for Excellence in Comparative Planetology, Hefei, China, ³Mengcheng National Geophysical Observatory, University of Science and Technology of China, Hefei, China, ⁴Center for Nonlinear Plasma Science and C.R. ENEA Frascati, Frascati, Italy, ⁵Institute of Fusion Theory and Simulation and Department of Physics, Zhejiang University, Hangzhou, China, ⁶Department of Physics and Astronomy, University of California, Irvine, CA, USA

Abstract Whistler mode chorus waves are quasi-coherent electromagnetic emissions with frequency chirping. Various models have been proposed to understand the chirping mechanism, which is a long-standing problem in space plasmas. Based on analysis of effective wave growth rate and electron phase space dynamics in a self-consistent particle simulation, we propose a phenomenological model called the “Trap-Release-Amplify” (TaRA) model for chorus. In this model, phase space structures of correlated electrons are formed by nonlinear wave particle interactions, which mainly occur in the downstream of equator. When released from the wave packet in the upstream, these electrons lead to selective amplification of new emissions which satisfy the phase-locking condition to maximize wave power transfer, resulting in frequency chirping. The phase-locking condition at the release point gives a chirping rate that is, fully consistent with the one by Helliwell in case of a nonuniform background magnetic field. The nonlinear wave particle interaction part of the TaRA model results in a chirping rate that is, proportional to wave amplitude, a conclusion originally reached by Vomvoridis et al. Therefore, the TaRA model unifies two different results from seemingly unrelated studies. Furthermore, the TaRA model naturally explains fine structures of chorus waves, including subpackets and bandwidth, and their evolution through dynamics of phase-trapped electrons. Finally, we suggest that this model could be applied to explain other related phenomena, including frequency chirping of chorus in a uniform background magnetic field and of electromagnetic ion cyclotron waves in the magnetosphere.

1. Introduction

Whistler mode chorus is one of the most intense naturally occurring electromagnetic emissions in planetary magnetospheres. These waves are practically important because they play key roles in energetic electron dynamics in the inner magnetosphere through resonant wave particle interactions, such as accelerating radiation belt electrons in the recovery phase of geomagnetic storms (Horne et al., 2005; Reeves et al., 2013; Thorne et al., 2013), or scattering plasmasheet electrons into the atmosphere to form diffuse and pulsating aurora (Kasahara et al., 2018; Nishimura et al., 2010; Thorne et al., 2010). Chorus waves are also scientifically interesting because they consist of narrowband quasi-coherent emissions with frequency chirping, which could occur in either upward (rising-tone) or downward (falling-tone) directions (Burtis & Helliwell, 1976; Tsurutani & Smith, 1974). The frequency chirping has also been found in other wave modes, such as electromagnetic ion cyclotron waves in the magnetosphere (Pickett et al., 2010) or Alfvén waves in fusion plasmas (Heidbrink, 1995), suggesting its universal presence. Correspondingly, understanding the chirping of chorus could be potentially beneficial to understanding a wide range of phenomena in both space and fusion plasmas, and is also the focus of this paper.

The chirping mechanism of chorus waves has been under intensive research and debate since 1960s (Demekhov, 2011; Helliwell, 1967; Nunn, 1974; Omura & Nunn, 2011; Omura et al., 2008; Sagdeev et al., 1985; Sudan & Ott, 1971; Trakhtengerts, 1995; Vomvoridis et al., 1982; Zonca et al., 2017). Helliwell (1967) proposed a phenomenological model to explain chirping by assuming a “consistent-wave” condition, in which the spatial variation of electron cyclotron frequency due to an inhomogeneous background magnetic field is matched by the Doppler shifted wave frequency to maximize wave power transfer. The chirping rate proposed in the model is proportional to the background magnetic field inhomogeneity and has been shown to be consistent with observation (Tao et al., 2012) and self-consistent particle-in-cell (PIC) simulations

(Tao, 2014). Nunn (1974) derived wave kinetic equations for narrowband emissions, and calculated the nonlinear resonant current due to phase-trapped electrons. Based on this analysis, the author developed a reduced numerical model called Vlasov Hybrid model, which is capable of simulating both rising tone and falling tone emissions (Nunn, 1990; Nunn et al., 1997). An equivalent model has also been applied to study nonlinear sideband instability and demonstrated the preference for upper sideband in a parabolic background magnetic field (Nunn, 1986). Assuming that chirping exists, Vomvoridis et al. (1982) suggested that the chirping rate is proportional to wave amplitude, based on the maximization of wave amplification due to nonlinear wave particle interactions. This relation has also been obtained by Omura et al. (2008) and Zonca et al. (2017) with different methods, and used by the backward wave oscillator model of chorus (Trakhtengerts, 1995) to obtain frequency chirping rate from the derived wave amplitude. It has also been verified directly by PIC simulations (Hikishima et al., 2009; Katoh & Omura, 2013; Tao et al., 2017b) and observations (Cully et al., 2011; Mourenas et al., 2015). Omura and Nunn (2011) proposed a sequential triggering model where chirping is caused by the nonlinear frequency shift due to the nonlinear current parallel to the wave magnetic field (δj_B). Zonca et al. (2017) proposed a self-consistent theoretical framework, in which chirping is due to the nonlinear excitation of a narrowband spectrum out of a broad and dense background whistler wave modes (see also, Chen & Zonca, 2016; Zonca, Chen, Briguglio, Fogaccia, Milovanov, et al., 2015).

Despite success of different chorus wave models in different aspects, various questions remain to be elucidated about the chirping process. First, if chirping is caused by the background magnetic field nonuniformity as in Helliwell (1967) or Sudan and Ott (1971), how to explain chirping in a uniform background magnetic field as demonstrated by first-principle PIC simulations (Wu et al., 2020) or the BWO model simulation (Demekhov & Trakhtengerts, 2008)? Second, the chirping rate has been shown to be a function of either the background magnetic field inhomogeneity (Helliwell, 1967) or the wave amplitude (Omura et al., 2008; Vomvoridis et al., 1982; Zonca et al., 2017). These two estimates of the chirping rate are very different, but both have been verified by observations and simulations (Cully et al., 2011; Katoh & Omura, 2011; Hikishima et al., 2009; Tao et al., 2012, 2017b; Titova et al., 2003). Is it possible for both chirping rate equations to be correct? If so, how to properly relate one to the other and what is the cause of the difference? A better understanding of the chirping process of chorus is crucial to resolve these seemingly inconsistent results.

In this work, based on detailed analysis of the spatial dependence of effective wave growth rate (Section 3) and electron phase space dynamics (Section 4) in a PIC simulation of chorus, and the theoretical framework of chorus by Zonca et al. (2017), we propose a “Trap-Release-Amplify” (TaRA) model to elucidate how and where chirping occurs (Section 5). The model naturally yields both chirping rates of chorus from Helliwell (1967) and Vomvoridis et al. (1982). Detailed comparison of the TaRA model with models proposed by Helliwell (1967) and Omura and Nunn (2011) is shown in Section 6. Application of the TaRA model to explain chorus subpackets and instantaneous bandwidth is discussed in Section 7. We summarize our main results and discuss possible applications of the TaRA model to other chirping phenomena in Section 8.

2. Simulation Setup

To simulate chirping elements of chorus, we use a 1D spatial, 3D velocity code named DAWN (Tao, 2014), originally developed after the 1D Electron Hybrid Model (Katoh & Omura, 2007) but later extended to use the nonlinear δf method (Hu & Krommes, 1994; Parker & Lee, 1993) to reduce simulation noise (Tao et al., 2017b). Cold electrons are represented using linearized fluid equations, and hot electrons are modeled by PIC techniques with the nonlinear δf method. The hot electron distribution is bi-Maxwellian with temperature anisotropy to provide the free energy for chorus excitation. Because whistler-mode chorus waves typically have a frequency much larger than the proton cyclotron frequency, ions are fixed. The background magnetic field is chosen to be of the parabolic form, $B = B_0(1 + \xi z^2)$. The flexible form of B can represent a dipole field near the equator (Helliwell, 1967; Katoh & Omura, 2007; Nunn, 1990), in which case the inhomogeneity parameter $\xi = 4.5/(LR_p)^2$ with L the L -shell and R_p the planet radius. It is also possible to investigate the controlling effects of magnetic field geometry on chorus chirping directions by changing the sign of ξ , as demonstrated by Wu et al. (2020). Only parallel propagating whistler waves are allowed in the DAWN code. Reflecting and absorbing boundaries conditions are used for particles and waves, respectively.

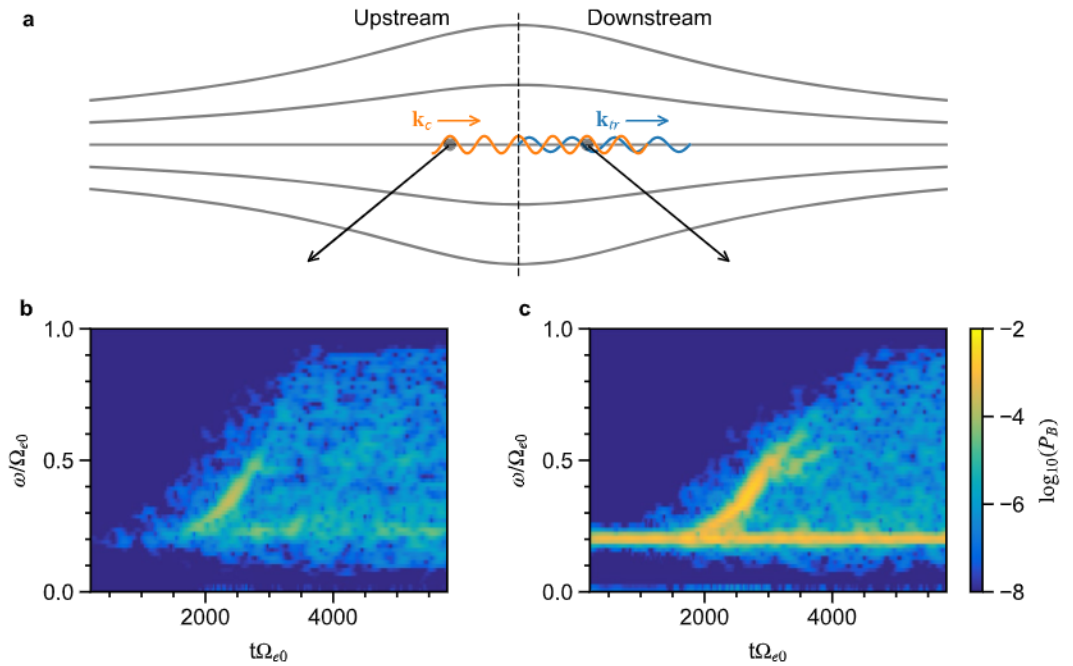


Figure 1. (a) Illustration of the particle-in-cell simulation setup, and the definition of “upstream” and “downstream” regions. The blue waveform (k_{tr}) represents the unidirectional triggering wave used in the simulation, and the orange waveform (k_c) represents the generated chorus element. The vertical dashed line marks the equator ($z = 0$). Example wave spectrograms showing chorus element in the (b) upstream and (c) downstream. Color-coded is the wave magnetic field power spectral density.

Our simulation setup is illustrated in Figure 1a. A rightward propagating (in $+z$ direction) triggering wave, represented by k_{tr} , is launched from the equator. A chirping element of chorus, represented by k_c , is generated in the “upstream” region. This chorus element propagates in the same direction as the triggering wave, a result of cyclotron resonance between parallel propagating whistler waves and electrons. Here “upstream” and “downstream” regions are defined relative to the wave propagation direction. The reason we use a unidirectional triggering wave at the equator is that we would like to clearly demonstrate that the excitation of chorus occurs in the upstream region, as shown in Figures 1b and 1c. The generation of chorus element only in one direction also helps analyzing wave growth rate and electron phase space dynamics. Strictly speaking, this simulation is about triggered emissions; however, our conclusions in the paper apply equally well to spontaneous chirping of chorus, in which case, the most unstable linear mode plays the role of the triggering wave, as noted by several previous studies (e.g., Katoh & Omura, 2007; Omura et al., 2008; Tao et al., 2020).

For our simulation, we use a time step $t\Omega_{e0} = 0.02$ and a grid size $\Delta z = 0.05d_e$ with $d_e \equiv c/\Omega_{e0}$ to accurately resolve the electron cyclotron motion and to satisfy the Courant condition. Here $\Omega_{e0} \equiv eB_0/mc$ is the equatorial electron cyclotron frequency, with $-e$ and m the electron charge and mass, respectively, and c being the speed of light in vacuum. Following previous studies (Tao et al., 2014, 2017a, 2017b), the cold plasma frequency is chosen to be $\omega_{pe} = 5\Omega_{e0}$, the ratio of hot to cold electron number density is 6%, and the background magnetic field inhomogeneity parameter $\xi = 2.155 \times 10^{-5} d_e^{-2}$. In total, we use 6,554 cells with 2,000 particles per cell to reduce simulation noise. The parallel and perpendicular thermal velocities are $0.2c$ and $0.3c$, respectively. The corresponding temperature anisotropy is smaller than the one used by our previous studies (Tao et al., 2014, 2017a, 2017b), so that no chirping elements can be generated without the triggering wave. Examples of chirping elements in the upstream and downstream regions can be found in Figures 1b and 1c.

3. Effective Growth Rate

We estimate the effective growth rate of chorus waves to demonstrate its spatial dependence and to help identify the wave generation region.

3.1. Method of Estimation

This effective growth rate (γ_{eff}) can be easily obtained from the wave kinetic equation

$$\frac{\partial W}{\partial t} + \frac{\partial}{\partial z}(v_g W) = 2\gamma_{\text{eff}} W, \quad (1)$$

as shown by several previous studies (Nunn, 1974; Shklyar, 2011; Shklyar & Matsumoto, 2009; Zonca et al., 2017), where W is the wave energy density, and v_g is the wave group velocity. It can also be obtained by noting that the time-averaged power transfer rate (P) is

$$\langle P \rangle = -\frac{1}{2} \text{Re}(\delta \mathbf{j}_h \cdot \delta \mathbf{E}^*), \quad (2)$$

where $\langle \dots \rangle$ represents averaging over fast wave oscillation period, $\delta \mathbf{j}_h$ and $\delta \mathbf{E}$ are complex notation of hot electron current density and wave electric field, respectively, with $\delta \mathbf{E}^*$ indicating the complex conjugate of $\delta \mathbf{E}$. The wave energy density, on the other hand, is given by (Tao et al., 2020; Stix, 1992, pp 75).

$$W = \frac{1}{16\pi} \frac{\omega}{v_g} \frac{\partial D}{\partial k} |\delta \mathbf{E}|^2 = -\frac{\omega}{16\pi} \frac{\partial D}{\partial \omega} |\delta \mathbf{E}|^2, \quad (3)$$

where in the last equation, we have used that $v_g = -(\partial D / \partial k) / (\partial D / \partial \omega)$ with k the wave number. Here

$$D = \frac{c^2 k^2}{\omega^2} - \left[1 - \frac{\omega_{pe}^2}{\omega(\Omega_e - \omega)} \right], \quad (4)$$

is the local dispersion function of parallel propagating whistler waves with $\Omega_e = eB/mc$ the local electron cyclotron frequency. Correspondingly, the effective growth rate is given by

$$\gamma_{\text{eff}} = \frac{\langle P \rangle}{2W} = \frac{4\pi}{\omega} \left(\frac{\partial D}{\partial \omega} \right)^{-1} \frac{\text{Re}(\delta \mathbf{j}_h \cdot \delta \mathbf{E}^*)}{|\delta \mathbf{E}|^2}, \quad (5)$$

and it is a time dependent function of ω and z . We would like to remark that whether γ_{eff} is nonlinear or not depends on the nonlinearity of $\delta \mathbf{j}_h$, or equivalently, the hot electron distribution function. We will now drop the subscript “eff” for simplicity.

As with other ways of obtaining growth rate in PIC type simulations, a reliable estimate depends on the signal-to-noise ratio. Therefore, as a consistency check, we also calculate the effective growth rate in a different way by using

$$W(z + \Delta z) = W(z) \exp \left[2 \int_z^{z+\Delta z} (\gamma' / v_g) dz' \right] \approx W(z) \exp \left[2 (\gamma' / v_g) \Delta z \right]. \quad (6)$$

Correspondingly,

$$\gamma' = \frac{v_g}{2\Delta z} \ln \left[\frac{W(z + \Delta z)}{W(z)} \right]. \quad (7)$$

A reliable estimate of effective growth rate would require that γ and γ' are consistent with each other. Otherwise, noise might dominate wave signal, and γ (or γ') cannot be used.

3.2. Variation of γ Along a Ray Path

We investigate the spatial dependence of γ and demonstrate generation of chorus in the upstream region by estimating γ for a representative frequency, $\omega = 0.34\Omega_{e0}$, along its raypath. This frequency is one of the frequencies from FFT and also about the frequency of maximum wave intensity, as indicated by the cross

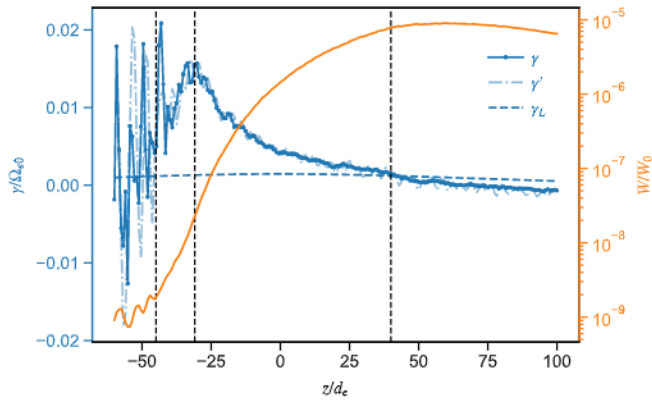


Figure 2. The spatial dependence of effective (γ and γ') and linear (γ_L) growth rates, shown in the left y-axis, and the wave energy density (W), shown in the right y-axis. The three vertical dashed lines mark the three characteristic locations discussed in the text, from left to right, $z/d_e = -45, -31$, and 40 .

sign in Figure 3b. We use 4,096 data points with $\Delta t = 0.1\Omega_{e0}^{-1}$ in all FFT calculations for wave spectrum and calculation of δj_h and δE used by Equation 5.

To find the raypath, we first locate the time t_0 of this ray arriving at $z = 0$, which is $t_0 \approx 2483\Omega_{e0}^{-1}$. Then using t_0 and $z = 0$ as the initial condition, we trace this ray both backward and forward in time to find its raypath for $-60d_e \leq z \leq 100d_e$ with 200 z 's; that is, $\Delta z = 0.8d_e$. Along its raypath, we calculate γ and γ' using Equations 5 and 7, respectively, and the wave energy density W using Equation 3. The results are shown in Figure 2. As a reference, we also calculate linear growth rate γ_L using the initial bi-Maxwellian distribution. From Figure 2, we note that the wave energy density W fluctuates for $z \lesssim -45d_e$, indicated by the left most dashed vertical line, consistent with that noise dominates for $z \lesssim -45d_e$ from wave spectrogram (e.g., see Figure 4). For $z \gtrsim -45d_e$, W continuously increases with z . Both growth rates γ and γ' fluctuate at large and negative z and show relatively good agreement with each other for $z \gtrsim -40d_e$. The two growth rates also show a local peak near $z = -31d_e$. In our discussion below, we will use $z = -31d_e$ as where the peak value of the effective growth rate is for simplicity and consistency.

Figure 2 clearly show three distinctive features of γ , especially when compared with γ_L . First, the maximum value of the effective growth rate is in the upstream region near $z = -31d_e$, not at the equator where the linear growth rate γ_L peaks. Starting from $z = -31d_e$, the effective growth rate γ decreases as the ray propagates downstream, and becomes smaller than γ_L for $z \gtrsim 40d_e$. Second, the effective growth rate γ is significantly larger than γ_L in the upstream, ensuring the growth of a narrowband emission out of linearly unstable broadband whistler mode waves. Third, the path-integrated convective wave growth rate, characterized by $G \equiv \int \gamma dz / v_g$, is much larger in the upstream region (from $z = -45d_e$ to $z = 0$), than that in the downstream region (from $z = 0$ to $z = 100d_e$). This can be directly calculated or can be seen from that $W(z = 0) \approx 1.4 \times 10^{-6}W_0$, $W(z = -45d_e) \approx 1.8 \times 10^{-9}W_0$, and $W(z = 100d_e) \approx 6.3 \times 10^{-6}W_0$, where $W_0 \equiv B_0^2/8\pi$ is the normalization unit of W . Correspondingly, $W(z = 0)/W(z = -45d_e) \approx 800$ and $W(z = 100d_e)/W(z = 0) \approx 5$. Clearly, the upstream region is significantly more effective at wave amplification than the downstream region. The asymmetry of γ and G with respect to $z = 0$ suggests that the upstream and downstream interaction regions might play very different roles in chorus wave generation.

3.3. Formation of the Chirping Element Using γ

One of the main principles of the theoretical framework of Zonca et al. (2017) is that chorus chirping observed at a given location is a result of continuous excitation of narrow spectrum out of a broad and dense background whistler modes. As a consistency check of this principle, we may use the effective growth rate calculated by Equation 5 to construct the power spectral density of wave magnetic field at $z = 0$ from $P_B(z = -50d_e)$ by

$$P'_B(\omega, z = 0) = P_B(\omega, z = -50d_e) \exp\left(2 \int_{-50d_e}^0 \gamma / v_g dz\right). \quad (8)$$

for all FFT frequencies below Ω_{e0} . It is important to note that, in the above equation, we use γ from Equation 5 instead of γ' in Equation 6. The wave power spectrum at $z = -50d_e$ is used because $P_B(z = -50d_e)$ related to the chirping element shows basically background thermal noise, as can be seen in Figure 3a. The relatively strong emission near $\omega/\Omega_{e0} \approx 0.2$ at $z = -50d_e$ in Figure 3a is due to the weak leftward propagating signal from the antenna being amplified by hot electrons. Applying Equation 8 to this signal will produce numerical artifact near $\omega/\Omega_{e0} \approx 0.2$ at $z = 0$ because v_g in Equation 8 is assumed to be positive in our calculation. This, however, does not affect our conclusions since we focus on reproducing the chorus chirping element, which propagates in $+z$ direction.

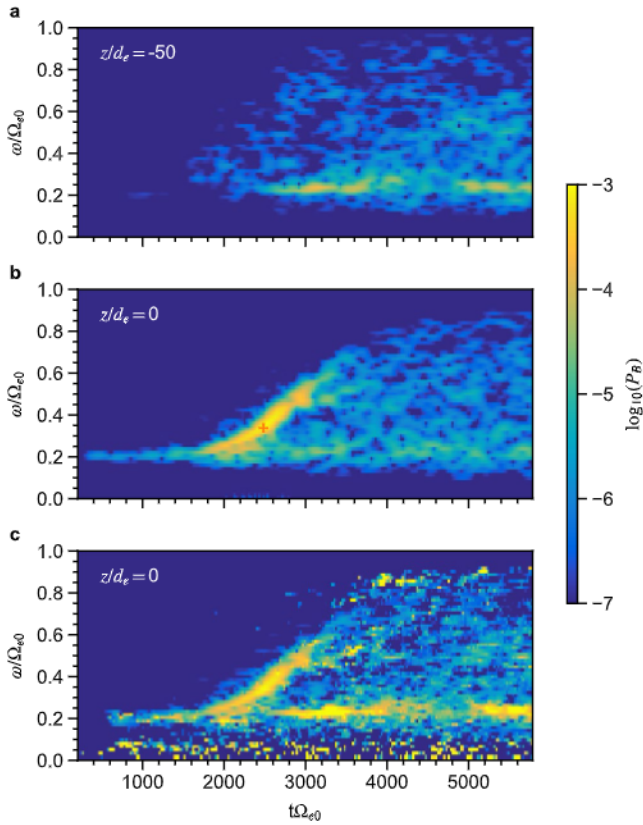


Figure 3. Wave power spectral density (P_B) at (a) $z/d_e = -50$ and (b) 0 from the particle-in-cell simulation, and (c) the constructed power spectral density (P'_B) using γ and $P_B(z/d_e = -50)$. The cross sign in Panel (b) indicates the initial time and frequency used in the calculation of raypath in Figure 2.

(Figure 4b). These two spectrograms suggest that the source location of the narrowband emission with $\omega = 0.34\Omega_{e0}$ is at $z/d_e < -40$. It is difficult to identify a chirping element at $z/d_e = -45$ in Figure 4c, and it is safe to say that at $z/d_e = -50$ (Figure 4d), the spectrogram along the raypath of the element shows basically thermal noise.

Combining the spectrograms in Figure 4 and the variation of γ and W shown in Figure 2, we conclude that the source region for generation of the emission with $\omega = 0.34\Omega_{e0}$ is located roughly between $z/d_e = -40$ and -50 .

3.5. Variation of R for Resonant Electrons

Having identified the source region, we now analyze the R parameter at wave generation. This parameter is important in studying nonlinear resonant wave particle interactions and is defined through the second order time derivative of wave particle interaction phase angle $\zeta \equiv \langle \mathbf{v}_\perp, \delta \mathbf{B} \rangle$. For resonant interactions between electrons and parallel whistler waves, the first order time derivative of ζ is

$$\frac{d\zeta}{dt} = \omega - kv_{\parallel} - \Omega_e \quad (9)$$

and its second order time derivative is

$$\frac{d^2\zeta}{dt^2} = \omega_{ir}^2 \sin \zeta - (R_1 + R_2), \quad (10)$$

Figures 3b and 3c show the comparison between wave spectrogram from DAWN simulation (Figure 3b) and the spectrogram constructed using Equation 8 (Figure 3c). Although part of spectrogram is clearly contaminated by noise in the calculated effective growth rate, it is quite obvious that Equation 8 is able to reproduce the main portion of the chirping element. This good agreement suggests that our estimated γ is quite reliable for most part of the element, but more importantly, it shows consistency with the theoretical framework of Zonca et al. (2017). Note that because v_g is independent of time in Equation 8, all the dynamics needed to produce frequency chirping is contained in the effective growth rate γ . Therefore, a plausible scenario is that narrowband emissions of different frequencies are excited at different times and locations, due to the spatial and temporal dependence of γ , in the upstream region. These narrowband emissions arrive at a given location at downstream at different times, leading to a chirping element with increasing frequency. A self-consistent description of how the nonlinear wave particle interactions modify the hot electron distribution function and the effective growth rate is given in the theoretical framework of Zonca et al. (2017).

3.4. Identification of the Source Region

The spatial profile of γ and W along the raypath shown in Figure 2 suggests that the generation of emission with $\omega = 0.34\Omega_{e0}$ occurs somewhere near $z/d_e = -40 \sim -50$. This could be further confirmed by plotting the spectrogram of waves at various locations. The principle of using wave spectrogram to constrain the source location is simple: for a given z_0 , if a clear signal of the given frequency $\omega = 0.34\Omega_{e0}$ along the raypath is identifiable, then this particular mode is generated at a location $z < z_0$, since waves of interest propagate in $+z$ direction.

Figure 4 shows four spectrograms at $z/d_e = -35, -40, -45$, and -50 . In Figure 4a, $z/d_e = -35$, we see a clear part of the chirping element including $\omega = 0.34\Omega_{e0}$. This element is also weakly visible at $z/d_e = -40$

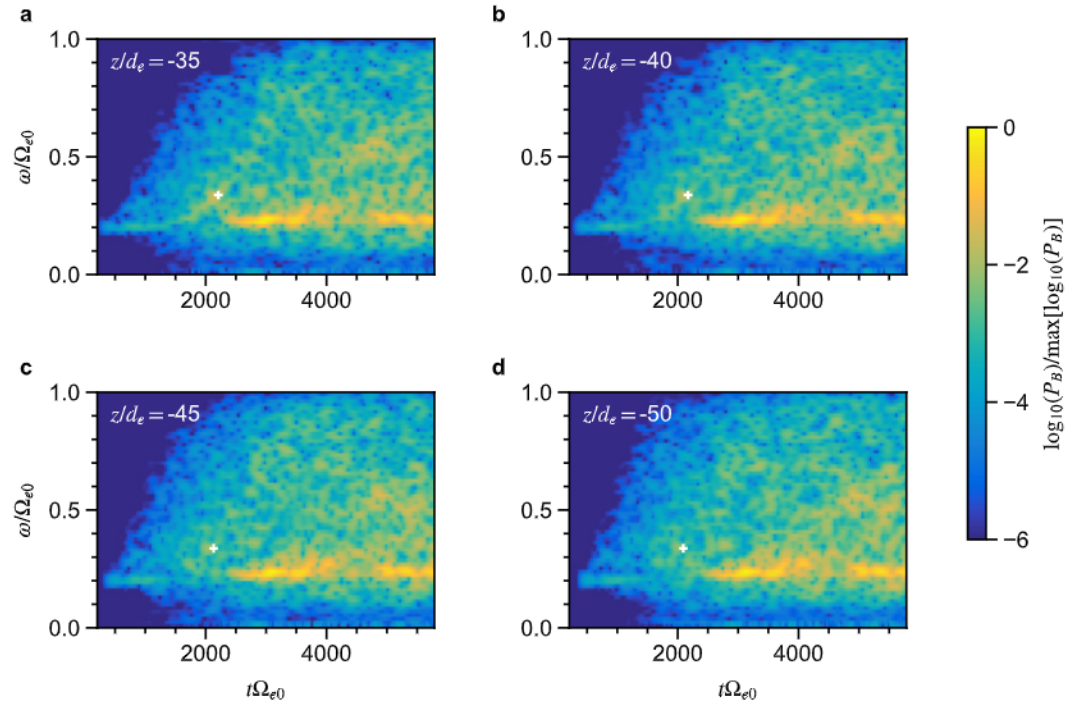


Figure 4. Wave power spectrograms at four different locations (z/d_e): (a) -35 , (b) -40 , (c) -45 , and (d) -50 . These spectrograms are used to help identify the source region of the emission with $\omega/\Omega_{e0} = 0.34$. The white cross marks the time and location of the ray at these four locations.

where

$$R_1 = \left(1 - \frac{v_r}{v_g}\right)^2 \frac{\partial \omega}{\partial t}, \quad (11)$$

$$R_2 = \left(\frac{kv_{\perp}^2}{2\Omega_e} - \frac{3v_r}{2}\right) \frac{\partial \Omega_e}{\partial z}. \quad (12)$$

Clearly R_1 characterizes effects of frequency chirping; R_2 , effects of background magnetic field inhomogeneity. In above equations, v_r is the resonant parallel velocity that gives $d\zeta/dt = 0$, v_{\perp} is the perpendicular velocity with respect to background \mathbf{B} , and $\omega_{tr}^2 = kv_{\perp}e\delta B/mc$ is the characteristic phase-trapping frequency. For convenience, we may also write ω_{tr} using normalized variables as

$$\left(\frac{\omega_{tr}}{\Omega_e}\right)^2 = \mu \left(\frac{\omega}{\Omega_e}\right) \left(\frac{v_{\perp}}{c}\right) \left(\frac{\delta B}{B}\right). \quad (13)$$

where $\mu \equiv ck/\omega$ is the refractive index. Relativistic effects could easily be included if needed. Equation 13 should be handy to quickly estimate ω_{tr} in various cases. The parameter R is defined by $R = (R_1 + R_2)/\omega_{tr}^2$.

The top panel of Figure 5 shows the variation of R together with the effective growth rate for $|z/d_e| \leq 60$, and the shaded region represents the range of z ($-50 \leq z/d_e \leq -20$) where ratios of $|R_2|$ and ω_{tr}^2 to R_1 are shown in the bottom panel. In calculation of R , we have used $\partial\omega/\partial t = 2.6 \times 10^{-4} \Omega_{e0}^{-2}$ estimated from wave spectrogram, and $\alpha \equiv \tan^{-1}(v_{\perp}/v_{\parallel}) = 70^\circ$, since it is most easily for phase-trapping to occur for particles with pitch angles near $65 - 75^\circ$ (Inan et al., 1978). Note that we use a constant α for simplicity of analysis, which means we do not follow a group of phase-trapped electrons between $z/d_e = -60$ and 60 when calculating R .

Figure 5 shows a few interesting features of R and the underlying electron dynamics. First, from $z = 0$ to $60d_e$, the value of R keeps decreasing from 0.35 to about 0.2 , suggesting stronger nonlinear wave particle

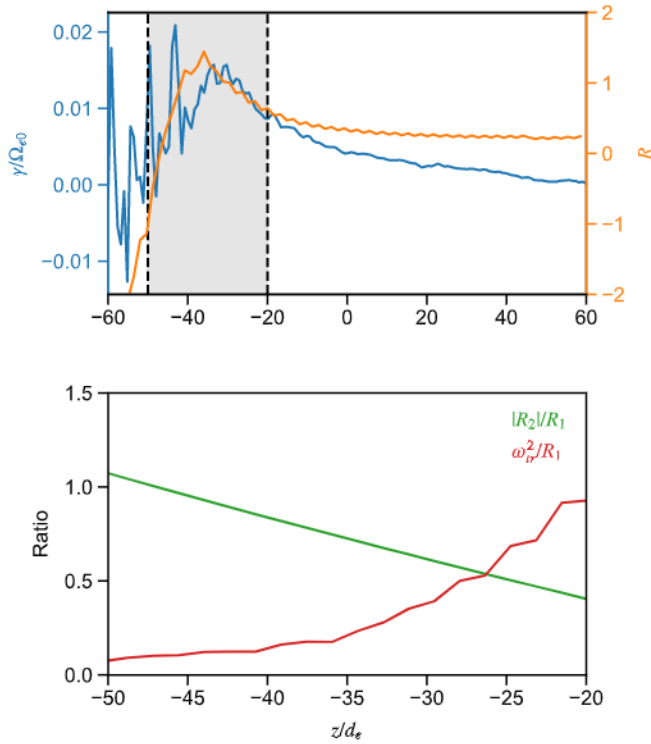


Figure 5. (Top) The spatial dependence of effective growth rate γ (the left y-axis) and R (the right y-axis) for $-60 \leq z/d_e \leq 60$. (Bottom) The spatial variation of the ratio $|R_2|/R_1$ (green) and ω_r^2/R_1 (red) for $-50 \leq z/d_e \leq -20$, the shaded region marked by the vertical dashed lines in the top panel.

interactions in the downstream than at the equator. Second, between $z = -30d_e$ and about $-40d_e$, $R \gtrsim 1$, suggesting that the wave is not effective at phase-trapping resonant electrons because of its weak amplitude. The value of R keeps decreasing to 0 and negative values as z further decreases. However, this does not mean that phase-trapping is possible again, because waves at these locations are broadband (e.g., see Figure 4d). The reason for R becoming 0 or negative can be seen from the bottom panel of Figure 5, which shows $|R_2|/R_1$ and ω_r^2/R_1 . From $z/d_e = -20$ to -50 , ω_r^2/R_1 decreases and $|R_2|/R_1$ increases, because of decreasing wave amplitude and increasing background field inhomogeneity, and the two ratios become comparable near $z/d_e \approx -26$. From $z/d_e = -40$ to -50 , which is about the source region of the emission with $\omega = 0.34$, $|R_2|/R_1$ changes from about 0.8 to 1 and ω_r^2/R_1 changes from about 0.1 to 0.05. Therefore, the value of R being close to 0 near $z/d_e \sim -50$ simply because R_1 nearly cancels R_2 . From $z/d_e = -40$ to -50 , we clearly have the following ordering between R_1 , R_2 and ω_r^2 : $R_1/R_2 \sim -1$ and $R_1, R_2 \gg \omega_r^2$. This is fully consistent with results of Wu et al. (2020), and suggests that

$$\frac{d^2\zeta}{dt^2} \approx -(R_1 + R_2) \approx 0, \quad (14)$$

from Equation 10. Physically, this means that the phase-locking condition, $d^2\zeta/dt^2 = 0$, could be satisfied through balancing R_2 by R_1 . As discussed below in Section 5, this can also be understood as a result of selective amplification of new emissions that can stay resonant ($d\zeta/dt = 0$) with these electrons for the longest possible time because of phase locking. Note that, phase-locked particles are not necessarily phase-trapped particles. On the other hand, among phase-trapped particles, those near the center of the island (the “O” point) are also phase-locked particles since $R \approx \omega_r^2 \sin^2 \zeta$, and therefore, $\ddot{\zeta} \approx 0$.

4. Electron Phase Space Dynamics

4.1. Entrapping and Detrapping of Resonant Electrons

Previous section analyzes the effective growth rate γ along a given raypath ($\omega = 0.34\Omega_{e0}$). Here we focus on a group of selected electrons, and demonstrate their trapping and release from the chorus wave packet in the downstream and upstream, respectively. We save 55 electron distributions equidistantly in time from $t\Omega_{e0} = 1,500$ to 5,500, or one distribution every $\sim 74\Omega_{e0}^{-1}$. One of the saved electron distributions is at $t\Omega_{e0} = 2241$, when γ of $\omega = 0.34\Omega_{e0}$ peaks near $z/d_e = -31$.

Figure 6 illustrates both the wave spectrograms (left column) and the phase space distributions of a group of selected electrons (375 in total) represented by red dots (right column) at three different locations. The criterion for selecting electrons is that they are located within the resonant island at $z/d_e = -4.5$ and $t\Omega_{e0} = 2092.6$ (Figure 6d). This particular time and location are used because most of these electrons would reach $z/d_e = -31$ near $t\Omega_{e0} = 2241$, responsible for the peaking of the growth rate of the mode with $\omega = 0.34\Omega_{e0}$. Backward from $z/d_e = -4.5$ by an equal amount of time, most electrons were located at $z/d_e = 30$, as shown in Figure 6b. The spectrograms in the left column show the frequency of maximum intensity of the chirping element at the three different times, indicated by vertical dashed lines. From the phase space plots of resonant islands in the right column, these frequencies are also resonant frequencies.

Figures 6b, 6d and 6f clearly illustrate how electrons get phase-trapped and released as they move from downstream to upstream and resonantly interact with a chorus packet with chirping frequency. At $z/d_e = 30$, only part of the selected electrons are phase-trapped and located within the resonant island of the wave with $\omega = 0.23\Omega_{e0}$. Because resonant electrons move in opposite direction to the chirping wave packet, as

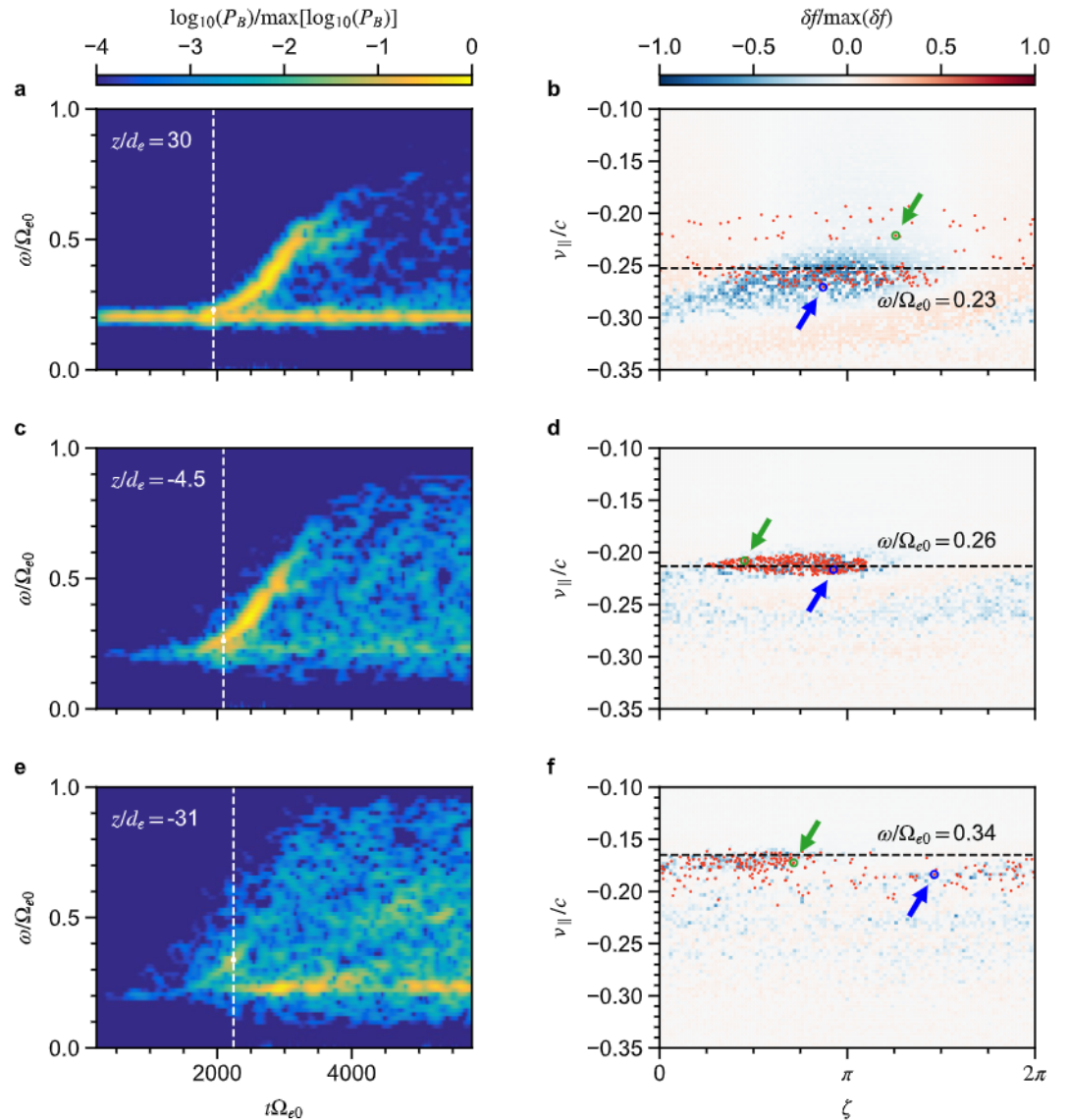


Figure 6. (Left) Wave spectrograms at three different locations (z/d_e): (a) 30, (c) -4.5, and (e) -31. (Right) The corresponding electron phase space ($v_{||}-\zeta$) distributions. In the left column, the vertical dashed lines mark the time of the corresponding phase space distribution. In the right column, the horizontal dashed lines mark the frequency of maximum wave intensity, and red dots mark phase space coordinates of selected electrons. The blue and green circles and arrows mark two electrons whose energy and phase angle variation are highlighted in Figure 7.

the selected electrons move upstream, the resonant frequency increases. At $z/d_e = -4.5$, all electrons are located within the resonant island and phase-trapped by the wave with $\omega = 0.26\Omega_{e0}$. Clearly, from $z/d_e = 30$ to -4.5 , the selected electrons experienced an entrapping process and become phase-organized. As the electrons arrive at $z/d_e = -31$ and the resonant frequency becomes $\omega/\Omega_{e0} = 0.34$, however, they start to get de-trapped as the calculated $R \sim 1$, although the selected electrons are still phase-correlated (Figure 6f). It is also clear that the selected electrons result in the amplification of the emission with $\omega/\Omega_{e0} = 0.34$, but are not responsible for its generation (see Section 3.4). As they move further upstream, the electrons will resonantly interact with waves whose frequency is higher than $0.34\Omega_{e0}$. Finally, we would likely to point out that, although the dynamics of only a selected group of electrons are analyzed, there is a continuous entrapping of fresh electrons in the downstream and release of these electrons in the upstream, responsible for continuous generation of new emissions. This mechanism can be viewed as the chorus wave packet slipping over the population of resonant electrons maximizing wave particle power extraction, and calls for the

analogy with super-radiance in free electron lasers introduced by Zonca, Chen, Briguglio, Fogaccia, Vlad, and Wang (2015) discussing energetic particle mode convective amplification in fusion plasmas. We shall come back to this point in the next section.

4.2. Variation of Wave Particle Interaction Phase Angle

The dynamics of resonant electrons demonstrated above clearly show similarities between chorus generation and various electronic devices, such as backward wave oscillators and free electron lasers. In fact, several authors have built chorus wave models based on the understanding of these devices which are capable of generating coherent emissions (Soto-Chavez et al., 2012; Trakhtengerts, 1995). In studies of wave generation in these devices, one important variable is how the wave particle interaction phase angle (ζ) changes during the whole interaction process. Here we show the variation of ζ of the selected electrons as they move from $z/d_e = 30$ to -31 , along with the energy change, as an indicator of phase-trapping. For simplicity of discussion, two electrons are selected, as indicated by the green and blue circles and arrows in Figure 6. These two electrons are from slightly different groups of selected electrons, and will be called blue and green electrons, respectively. The blue electron represents those that are already phase-trapped at $z/d_e = 30$, and the green electron represents those that are untrapped at $z/d_e = 30$ but get phase-trapped somewhere between $z/d_e = 30$ and -4.5 .

Figures 7a and 7b show the energy change, $\Delta\mathcal{E} \equiv \mathcal{E}(t) - \mathcal{E}(t = 0)$, and the ζ change, $\Delta\zeta \equiv \zeta(z) - \zeta(z = -4.5)$, of all selected electrons, respectively. Note that different types of reference values are used for $\Delta\mathcal{E}$ and $\Delta\zeta$: $\Delta\mathcal{E}$ is the energy change from its initial value, while $\Delta\zeta$ is the phase angle change with respect to $z/d_e = -4.5$, near the equator. The energy change of the blue electron in Figure 7a suggests that this electron got phase-trapped at about $t\Omega_{e0} \approx 1700$. Similarly, the green electron got phase-trapped at about $t\Omega_{e0} \approx 2000$. This is consistent with the much slower change of ζ for the blue (green) electron from $t\Omega_{e0} \approx 1700$ (2000) to about 2,241 than the rest of the time. Figure 7a also suggests that $\Delta\mathcal{E}$ is much larger for the blue electron than for the green electron, due to longer time of phase-trapping. One thing worth pointing out here is the much larger energy oscillation near $t\Omega_{e0} \approx 1700$ than at later times. This is consistent with the much larger amplitude modulation of waves in the downstream region as discussed in Section 7.

Figures 7c and 7d show the histogram of $\Delta\zeta$ at $z/d_e = 30$ and -31 . The median value of $\Delta\zeta$ is -2.12π at $z/d_e = 30$ and -0.74π at $z/d_e = -31$. The large variance of both statistics is associated with the fact that only part of the electrons are phase-trapped at $z/d_e = 30$ and part of the electrons get de-trapped slightly before reaching $z/d_e = -31$. Note the definition of $\Delta\zeta$, we may conclude that as electrons move from $z/d_e = 30$ to -4.5 , ζ increases by about 2π , and as they move from $z/d_e = -4.5$ to -30 , ζ decreases by about 0.7π .

These results are consistent with the analysis presented in Section 4.1 and can be interpreted as electrons in the downstream region forming a phase space structure when moving from $z/d_e = 30$ to $z/d_e = -4.5$ (cf. Figure 6) as they slip over the propagating chorus wave packet. Then, they are released from the structure as they reach $z/d_e = -31$ being phase shifted by $\sim -\pi$. The close analogy with super-radiance in free electron lasers (Zonca, Chen, Briguglio, Fogaccia, Milovanov, et al., 2015; Zonca, Chen, Briguglio, Fogaccia, Vlad, & Wang, 2015) is apparent when comparing panels (b) and (d) of Figure 6 with panels (a) and (b) of Figure 3 in Giannessi et al. (2005). Note that, in the case of Figure 7, we have focused the attention on two particles gaining energy from the interaction with the chorus element. However, the majority of electrons in the downstream region do the opposite, resulting in the overall amplification of the wave-packet; similar, again, to the free electron laser case.

5. A “Trap-Release-Amplify” (TaRA) Model

Combining results from Sections 3 and 4, we now describe a phenomenological model of chorus, called the TaRA model. This model explains how chirping occurs and relates the chirping rate of chorus to both the background magnetic field inhomogeneity and to wave amplitude.

Figure 8 illustrates the model, which shows the waveform of chorus at a given time taken from simulation, along with the background magnetic field. We assume that a chorus wave packet consists of a nearly

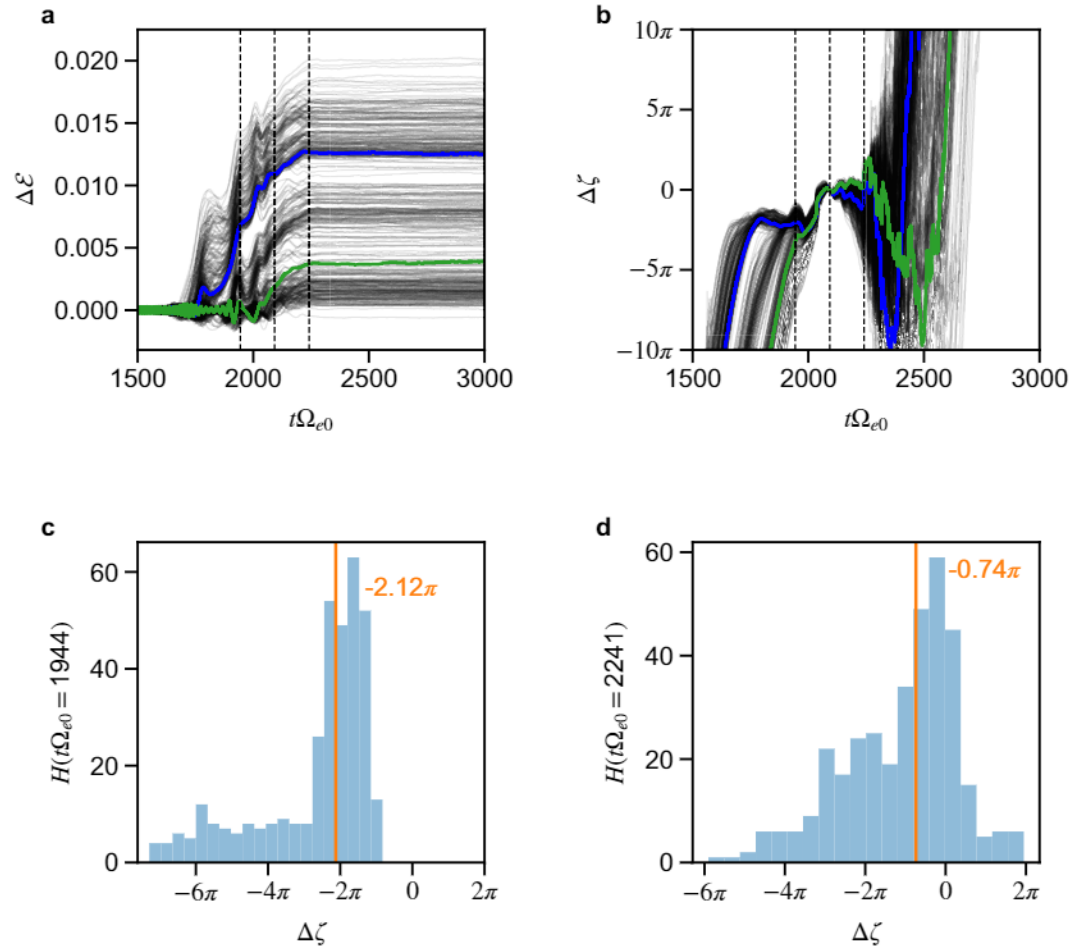


Figure 7. Variation of energy (\mathcal{E}) and ζ of all selected electrons. (a) Energy change from its initial value. (b) Phase angle change with respect to $\zeta(z/d_e = -4.5)$. (c) Histograms of $\Delta \zeta$ at $z/d_e = 30$. (d) Similar to (c), but at $z/d_e = -31$. In (a) and (b), the blue and green lines are for the electrons marked by blue and green circles in Figure 6.

continuous spectrum of whistler modes $\omega_0, \omega_1, \omega_2, \dots$, with $\omega_0 < \omega_1 < \omega_2 < \dots$. The spacing between these frequencies is infinitely small. We further assume that the generated part of the packet consists of modes with frequency from ω_0 to ω_N , and modes with $\omega_i, i > N$ are yet to be excited. For a rising-tone chirping element, clearly ω_0 is located in the front of the packet; ω_N , the rear of the packet.

Because of the opposite movement of resonant electrons and wave packet, the resonant interaction between fresh electrons and the generated part of the chorus packet starts from ω_0 in the downstream. These electrons get phase-trapped in the interaction process as they move toward the upstream, producing a “phase-bunched” current. As the electrons move to a region in the upstream such that the wave amplitude is too small to continue phase-trapping, the resonant electrons are released. Note that these electrons are still phase-correlated, and once released, they can selectively amplify new emissions ($\omega > \omega_N$) from the broadband background whistler wave spectrum based on the phase-locking condition: $d^2\zeta/dt^2 = 0$. This selection rule ensures that the resonance condition $d\zeta/dt = 0$ can be maintained for the longest possible time, therefore maximizes power transfer to the wave.

Based on this model, a few equations about chorus frequency chirping rate can be obtained. First, at the release point (Point 1 in Figure 8) where new emissions are excited, the wave amplitude term ω_r^2 is much smaller than the nonuniformity term, R_2 . Correspondingly, the phase locking condition requires balancing $-R_2$ by R_1 ; that is,

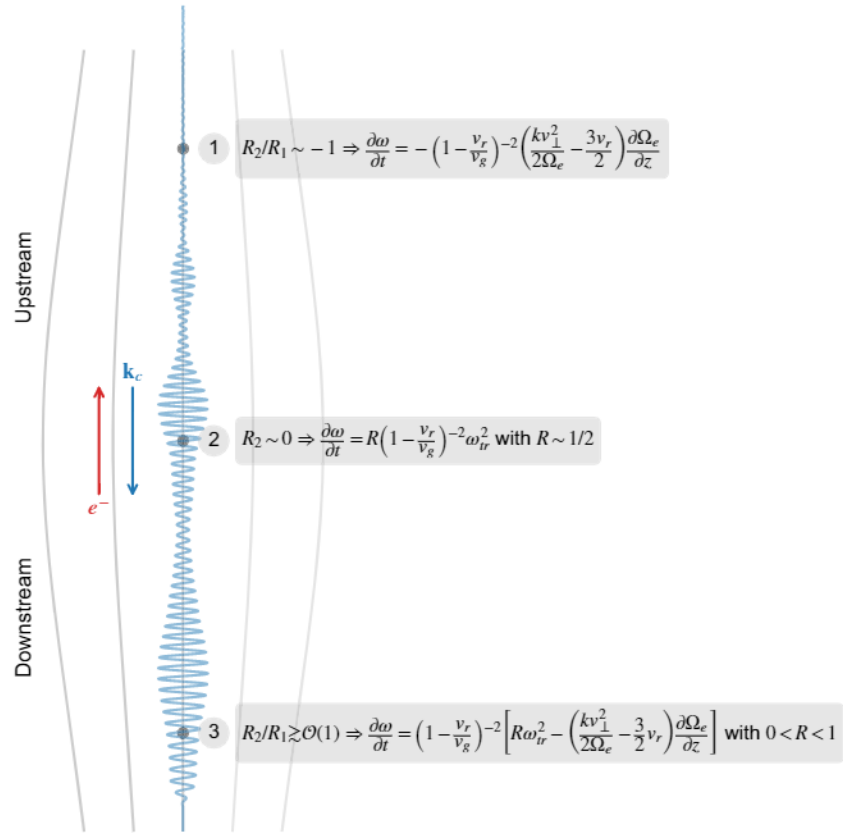


Figure 8. Illustration of the TaRA model. The red arrow indicates the motion of resonant electrons (e^-), while the blue arrow indicates the direction of wave vector (k_c) of chorus. The blue waveform is taken from simulation. Points 1, 2, 3 represent the release point ($R_2 \gg \omega_{tr}^2$), the equator ($R_2 = 0$), and a point in the downstream where $R_2/R_1 \gtrsim \mathcal{O}(1)$. The corresponding equations for the chirping rate are also given at the three points.

$$\frac{d^2 \zeta}{dt^2} = 0 \Rightarrow R_1 \sim -R_2, \text{ if } R_2 \gg \omega_{tr}^2, \quad (15)$$

which leads to,

$$\frac{\partial \omega}{\partial t} = - \left(1 - \frac{v_r}{v_g} \right)^{-2} \left(\frac{kv_{\perp}^2}{2\Omega_e} - \frac{3v_r}{2} \right) \frac{\partial \Omega_e}{\partial z}, \quad (16)$$

where we have used definitions of R_1 and R_2 in Equations 11 and 12. Equation 16 clearly defines a relation between the chirping rate and the background magnetic field inhomogeneity. In fact, according to our discussion above, we may say that, for the particular case of the rising-tone emission with $k > 0$, the negative inhomogeneity in the upstream region is the reason for the upward chirping of frequency. Second, the nonlinear phase-trapping of electrons caused by the generated part of the packet mainly occurs in the downstream region. Near the equator, $R_2 \sim 0$ (Point 2 in Figure 8). Based on the study of Vomvoridis et al. (1982), effective wave power transfer typically occurs for R between about 0.2 and 0.8. For simplicity, R is taken to be 1/2 as in Vomvoridis et al. (1982). Similar conclusion has also been reached by Omura et al. (2008) ($R = -0.4$), based on an assumed form of distribution for phase trapped electrons, and Zonca et al. (2017), based on a self-consistent theoretical framework of chorus. This leads to the well-known relation between the frequency chirping rate and the wave amplitude,

$$\frac{\partial \omega}{\partial t} = R \left(1 - \frac{v_r}{v_g} \right)^{-2} \omega_{tr}^2, \text{ with } R \sim \frac{1}{2}. \quad (17)$$

We must emphasize that, however, new emissions of the chorus packet are generated at Point 1 in Figure 8, not at the equator. Correspondingly, Equation 16 describes how frequency chirping occurs and why it is rising-tone in the current case, while Equation 17 emphasizes the importance of nonlinear wave particle interactions in chorus generation. Finally, in the downstream region at Point 3, where R_2 is comparable to or larger than R_1 , the contribution of the inhomogeneity term in calculation of R cannot be ignored, resulting in that

$$\frac{\partial \omega}{\partial t} = \left(1 - \frac{v_r}{v_g}\right)^{-2} \left[R \omega_r^2 - \left(\frac{kv_{\perp}^2}{2\Omega_e} - \frac{3v_r}{2} \right) \frac{\partial \Omega_e}{\partial z} \right], \quad (18)$$

with $0 < R < 1$ if the wave particle interaction is nonlinear.

From our description above, it is clear that the TaRA model shares a basic principle with most of previously published models of chorus (Helliwell, 1967; Nunn, 1974; Omura et al., 2008; Vomvoridis et al., 1982); that is, nonlinear wave particle interactions phase organize resonant electrons, allowing generation of narrowband coherent emissions. The difference among various models is mainly about how this principle is applied to explain chirping, to determine the chirping rate, and to explain various fine structures of chorus. Before detailed comparisons with previous models in Section 6, we would like to point out that, in the TaRA model, the chirping rate is related to both the background magnetic field inhomogeneity as by Helliwell (1967) in the upstream source region and to the wave amplitude as by Vomvoridis et al. (1982) at the equator. Correspondingly, our model unifies previous conclusions from two seemingly unrelated models (Helliwell, 1967; Vomvoridis et al., 1982) for the first time, as far as we are aware of. The difference in two ways of estimating chirping rate, Equations 16 and 17, is mainly caused by that they are derived at different stages of chorus generation, as illustrated in Figure 8.

6. Comparison With Previous Models

In this section, we compare in detail the TaRA model with two previous models. One is Helliwell's model (Helliwell, 1967), because the "consistent-wave" condition assumed by Helliwell's model to explain chirping is simply a special case of the general phase-locking condition used by the TaRA model, despite differences in other aspects of the models. The second one is the sequential triggering model (Omura, 2021; Omura & Nunn, 2011), because it is one of the most influential models in recent years.

6.1. Helliwell's Model

First, we demonstrate that Equation 16 could be written in exactly the same form as the one given by Helliwell (1967). Using the resonance condition $\omega - kv_r = \Omega_e$, we can write

$$-\left(\frac{kv_{\perp}^2}{2\Omega_e} - \frac{3}{2}v_r \right) = \frac{3v_r}{2} \left(1 + \frac{1 - \omega/\Omega_e}{3} \tan^2 \alpha \right). \quad (19)$$

With $v_g/v_r = -2\omega/\Omega_e$ for $\mu \gg 1$, it is straightforward to demonstrate that

$$\left(1 - \frac{v_r}{v_g} \right)^{-2} = -\frac{3\omega/\Omega_e}{1 + 2\omega/\Omega_e} \frac{v_g}{1 - v_g/v_r} \frac{2}{3v_r}. \quad (20)$$

Substituting Equations 19 and 20 into Equation 16, we arrive at

$$\frac{\partial \omega}{\partial t} = -\frac{v_g}{1 - v_g/v_r} \frac{3\omega/\Omega_e}{1 + 2\omega/\Omega_e} \left(1 + \frac{1 - \omega/\Omega_e}{3} \tan^2 \alpha \right) \frac{\partial \Omega_e}{\partial z}. \quad (21)$$

This equation is in exactly the same form as Equation 14 of Helliwell (1967), after taking into consideration the difference about signs of v_g and v_r in this paper and Helliwell (1967).

The agreement between Equations 16 and 21 is not surprising if one realizes that the phase locking condition with $R_2 \gg \omega_r^2$ is exactly the same as the "consistent-wave" condition used by Helliwell (1967), who requires

that the Doppler shifted wave frequency changes to match the spatial variation of the background electron gyrofrequency. The two models, therefore, share the same principle that frequency chirping results from the maximization of wave power transfer. On the other hand, Helliwell's model could be regarded as a special case of the TaRA model when nonuniformity (R_2) dominates nonlinearity (ω_r^2). This could be seen from that Helliwell's model does not allow chirping when the background magnetic field is uniform ($R_2 = 0$), as can be seen from Equation 21. However, in this case, it is still possible for R_1 to be balanced by the ω_r^2 term to achieve phase-locking in the TaRA model. The phase locking condition ($d^2\zeta/dt^2 = 0$) cannot be reduced to Equation 14, but is equivalent to

$$\frac{d^2\zeta}{dt^2} = \omega_r^2 \sin \zeta - R_1 = 0. \quad (22)$$

This suggests the possibility of frequency chirping in a uniform background magnetic field, as demonstrated by Wu et al. (2020). Correspondingly, the chirping in a uniform magnetic field might be considered as the case where nonlinearity (ω_r^2) dominates nonuniformity (R_2), opposite to the case discussed by Helliwell (1967) and the rest part of this paper. Application of the TaRA model to chirping in a uniform field is left as a future study.

In general, the location z_0 , used to evaluate $\partial\Omega_e/\partial z$ in Equations 21 or 16, needs to be calculated by taking into account the whole history of nonlinear wave particle interactions in both downstream and upstream. However, because electrons mainly get de-trapped in the upstream and the wavefield in the upstream is weak, it is possible to assume adiabatic motion of electrons in the upstream and obtain the lowest order estimate of z_0 , as done by Helliwell (1967). Correspondingly, we may use $|z_0| = (2\pi |v_{\parallel}|/\xi\Omega_{e0})^{1/3}$ from Helliwell (1967) in Equation 16 or Equation 21. This value of z_0 corresponds to a change of the wave particle interaction phase angle by π due to adiabatic motion of electrons and the background magnetic field non-uniformity (see also Figure 7). For the case in this study, $z_0 \approx -39d_e$, given that $v_r/c \approx -0.2$ for $\mu \approx 10$ and $\omega/\Omega_{e0} = 0.34$ at the equator. The estimated $\partial\omega/\partial t = 2.2 \times 10^{-4} \Omega_{e0}^{-2}$ with $\alpha = 70^\circ$. This is consistent with the measured chirping rate from the spectrogram at $z = 0$ for $\omega/\Omega_{e0} = 0.34$, which is $2.6 \times 10^{-4} \Omega_{e0}^{-2}$.

Equation (21) from Helliwell (1967) has been shown to agree well with observations (Tao et al., 2012) in terms of the dependence of $\partial\omega/\partial t$ on radial distance. The value of $\partial\omega/\partial t$ directly from Helliwell's model is about a factor of 2 smaller than observations. However, as pointed out by Tao et al. (2012), this is probably due to the working value of α being 30° from Helliwell (1967), who assumed an isotropic pitch angle distribution and complete bunching for simplicity. If one takes into consideration that nonlinear wave particle interaction most easily occurs for high pitch angles (Inan et al., 1978) and use, for example, $\alpha = 72^\circ$, the overall discrepancy between $\partial\omega/\partial t$ given by Equation 21 and observation is about 3% (Tao et al., 2012). Since Equation 16 of the TaRA model is the same as Equation 21 from Helliwell's model, and nonlinear wave interaction is taken into account ($\alpha \sim 70^\circ$), the results of Tao et al. (2012) also provide an observational support for the TaRA model.

In Helliwell's model, different tones are generated by shifting the interaction region to appropriate locations through the balance between input and output power. However, in PIC simulations, only rising-tone chorus has been reproduced so far with a dipole type background magnetic field (Katoh & Omura, 2007; Ke et al., 2017; Tao, 2014). For a given inhomogeneity factor ξ , decreasing or increasing linear drive will only produce featureless weak or strong broadband emissions, respectively (Katoh & Omura, 2013; Tao et al., 2014, 2020). Instead, spontaneous falling tone chorus has only been reproduced in PIC simulations with a reversed dipole magnetic field ($\xi < 0$), as demonstrated by Wu et al. (2020). Correspondingly, generation of various forms of chirping elements through shifting the interaction region back and forth via power balance is not part of the TaRA model for spontaneous chorus.

Other differences between the two models is about the extremely important role of nonlinear wave particle interactions, which result in $\partial\omega/\partial t \propto \delta B$ near the equator as illustrated in Figure 8. The nonlinear phase space dynamics of electrons also naturally explains the observed fine structures of chorus, such as chorus subpackets and the narrow bandwidth (see Section 7). Of course, the nonlinear wave particle interaction theory might not be well developed and the subpacket of chorus (Santolík et al., 2004, 2014; Tsurutani et al., 2020) was probably not known in 1960s.

6.2. The Sequential Triggering Model

Another very influential model which explains chorus chirping is by Omura and Nunn (2011), called the sequential triggering model (see also Katoh & Omura, 2013 and Shoji & Omura, 2013). In this model, the frequency chirping is due to the current parallel to the wave magnetic field, δj_B , by

$$c^2 k^2 - \omega^2 - \frac{\omega \omega_{pe}^2}{\Omega_e - \omega} = \mu_0 c^2 k \frac{\delta j_B}{\delta B}. \quad (23)$$

Note that, for consistency with Omura and Nunn (2011), SI units are used in this subsection, while the rest of the paper uses Gaussian-cgs units. By fixing k , a nonlinear resonant current δj_B due to phase trapped electrons leads to a frequency increase $\delta\omega$ from the frequency of the triggering wave ω . The triggered wave has frequency $\omega + \delta\omega$, and at the same time, a subpacket is formed. The new wave with frequency $\omega' = \omega + \delta\omega$ in turn plays the role of triggering wave, phase traps electrons forming δj_B , and changes frequency to $\omega' + \delta\omega'$. This triggering process occurs sequentially and forms a train of subpackets. Note here that $\delta\omega$ and $\delta\omega'$ are on the order of the frequency change over a subpacket, different from the infinitely small frequency spacing between modes ($\omega_i - \omega_{i-1}$) in the description of the TaRA model in Section 5.

Both the TaRA model and the sequential triggering model emphasize the key role of nonlinear wave particle interactions in chorus chirping and share the same relation between $\partial\omega/\partial t$ and δB , Equation 17. However, there are three main differences between the two models. First, the most fundamental difference is about how chirping occurs. In the TaRA model, frequency chirping is due to the selective amplification of new emissions which satisfy the phase-locking condition to maximize power transfer at the release point in the upstream. This allows us to relate both the frequency chirping rate and its direction to the background field inhomogeneity, Equation 16. In the sequential triggering model, the chirping occurs due to δj_B , which is formed by nonlinear wave particle interactions near the equator (Omura & Nunn, 2011). The chirping rate is related only to the wave amplitude as in Equation 17, a result from Omura et al. (2008), but not directly to the background magnetic field inhomogeneity. Second, in the sequential triggering model, each newly generated wave at ω' in turn plays the role of the triggering wave that phase-traps electrons to change the wave frequency until $\omega' + \delta\omega'$. In the TaRA model, all generated part of the chorus wave packet, from ω_0 to ω_N as in Section 5, could participate in nonlinearly phase-trapping new electrons to generate new emissions (Figure 8). Third, chorus subpacket is formed during the chirping process in the sequential triggering model. Each frequency sweeping from ω to $\omega + \delta\omega$ forms a subpacket. In this sense, chorus subpacket can be considered as the basic unit of wave excitation (Hanzelka et al., 2020; Katoh & Omura, 2013; Shoji & Omura, 2013). However, in the TaRA model, subpackets are formed by the conservation of momentum and energy between waves and phase-trapped electrons, see Section 7 or Tao et al. (2017a). Therefore, chorus subpackets are more prominent in the downstream and its period could change with wave amplitude as waves are nonlinearly amplified while propagating downstream.

We note that Shoji and Omura (2013) applied the sequential triggering model to EMIC waves and took into consideration the generation of new emissions in the upstream, as observed in their PIC-type simulations. Following Shoji and Omura (2013), Hanzelka et al. (2020) developed a model of subpackets based on the sequential triggering model, which also has the feature of wave generation in the upstream. Unlike the TaRA model, however, the generated new emission is not due to the selective amplification through phase-locking at the release point, but due to δj_B formed by nonlinear interactions with the previous triggering wave at the previous triggering point. Besides, both results of Hanzelka et al. (2020) and Shoji and Omura (2013) are based on the sequential triggering model; therefore, comments above about the differences between the two models regarding how chirping and subpackets occur still apply.

7. Fine Structures of Chorus

7.1. Chorus Subpackets

In the TaRA model, chorus subpackets are explained by conservation of momentum and energy between wave fields and phase-trapped electrons (Tao et al., 2017a). As phase-trapped electrons rotate in phase space, their velocity, and hence momentum, oscillates quasi periodically with period of $\mathcal{O}(\omega_r^{-1})$. Conservation of momentum between waves and electrons naturally leads to that the wave amplitude oscillates at $\mathcal{O}(\omega_r^{-1})$

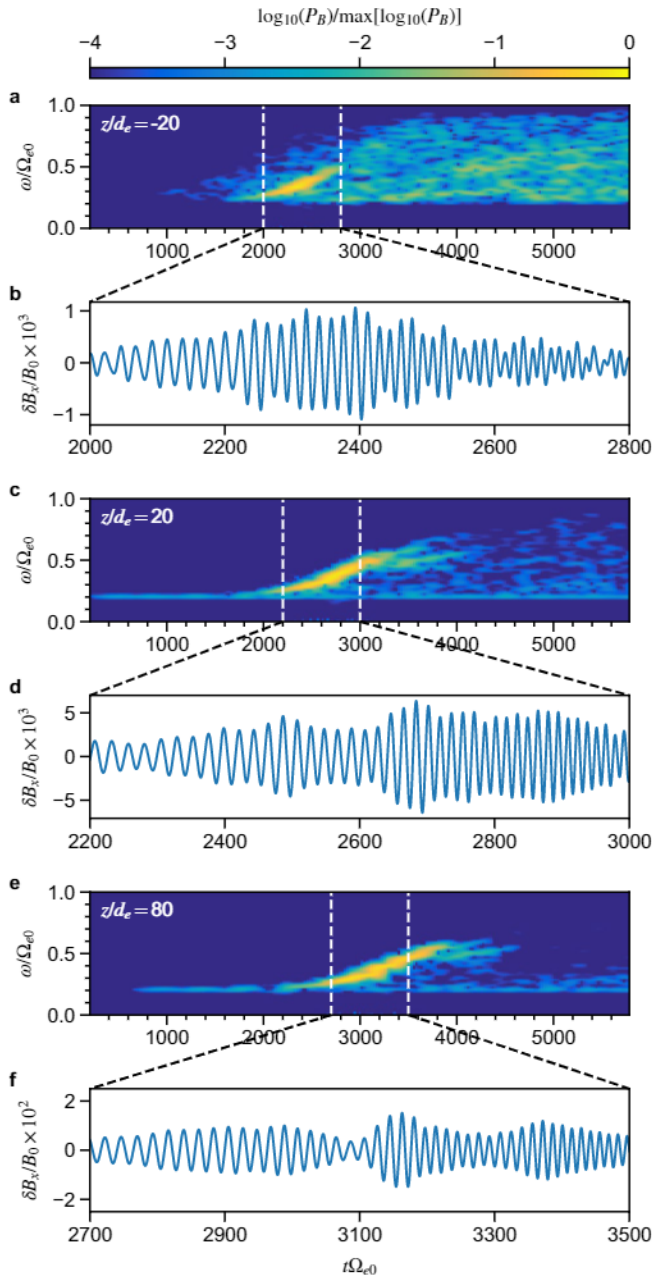


Figure 9. Comparison of chorus waveforms at $z/d_e = -20, 20$, and 80 , together with corresponding wave spectrograms. In (a), (c), and (e), color-coded is the normalized wave power spectral density.

(O’Neil, 1965; Tao et al., 2017a, 2020). Based on this explanation of the subpackets, we can immediately arrive at a few conclusions as follows.

First, in the TaRA model, there could be amplitude variation with frequency in the upstream due to the frequency dependence of the growth rate. However, since phase trapping mainly occurs in the downstream, so are the quasi-periodic chorus subpackets. This is illustrated in Figure 9, where we show waveforms at three different locations: $z/d_e = -20, 20$, and 80 . We have bandpass filtered the waveform using Butterworth filter to remove the triggering wave at $0.2\Omega_{e0}$. At $z/d_e = -20$, there is no obvious quasi-periodic variation of wave amplitude. However, in the downstream region, the subpackets are clearly visible at $z/d_e = 20$ and even more so at $z/d_e = 80$.

Second, the number of subpackets within one element is not fixed, but could change as wave amplitude changes. Suppose the starting and ending frequencies of an element is ω_i and ω_f , respectively, then the number of subpackets within one element, N_s , is

$$N_s \sim (\omega_f - \omega_i) \left(\frac{\partial \omega}{\partial t} \frac{2\pi}{\omega_r} \right)^{-1}. \quad (24)$$

Note that here we cannot use Equation 17 to arrive at the conclusion that N_s is proportional to ω_r^{-1} or $\delta B^{-1/2}$. This is because Equation 17 is valid only near the equator. Once generated, the frequency chirping rate does not change much (e.g., by dispersion) in the equatorial region. Correspondingly, we would arrive at $N_s \propto \omega_r \propto \delta B^{1/2}$. This suggests that as waves propagate downstream and get amplified, the number of subpackets increases weakly with increasing δB , as long as the interaction remains nonlinear. This is not obvious in Figure 9, because the wave amplitude increases only by about a factor $2 \sim 3$. However, this might provide a possible explanation for the observed short and intense subpackets within a chorus element (Nunn et al., 2021; Zhang et al., 2018, 2019), which play important roles in nonlinear acceleration of radiation belt electrons (Artemyev et al., 2020; Mourenas et al., 2018).

Third, the depth of modulation measured by $\delta B_{\max} - \delta B_{\min}$ is not fixed, but related to the magnitude of total momentum change during half the trapping period, Δp , of all phase-trapped particles. The deeper wave amplitude modulation in the downstream is clearly consistent with the larger energy and momentum variation of phase-trapped electrons, as demonstrated in Figure 7a. The cause of this might be related to the larger wave amplitude in the downstream, as can be argued as follows. The exact calculation of Δp is complicated in case of a fast chirping chorus element. But qualitatively, it could be expressed as

$$\Delta p \sim |\overline{\delta p_+} N_+ - \overline{\delta p_-} N_-|, \quad (25)$$

where $\overline{\delta p_+}$ ($\overline{\delta p_-}$) is the average amount of momentum increase (decrease) per trapped particle during half the trapping period, and N_+ and N_- are the related number of particles. For simplicity of discussion, we assume $\overline{\delta p_+} = \overline{\delta p_-} = \overline{\delta p}$; therefore,

$$\Delta p \sim |\overline{\delta p} \times \Delta N|, \quad (26)$$

where $\Delta N \equiv N_+ - N_-$, which is clearly related to the phase space density gradient at the resonant velocity. If, for example, after sufficiently phase-mixing such that the phase-space density within the trapping region is constant, then $\Delta N = 0$ and there is no amplitude modulation. On the other hand, δp is related

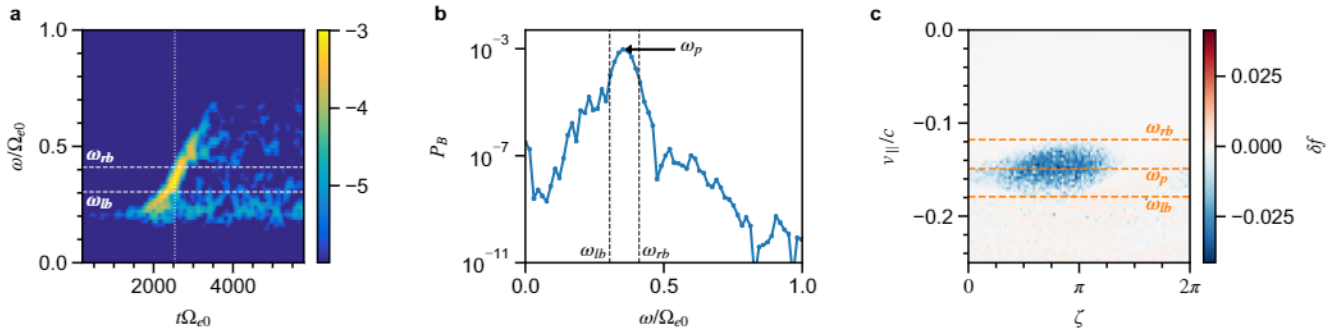


Figure 10. Estimation of the instantaneous bandwidth of chorus. (a) The wave spectrogram at $z/d_e = 0$. (b) The power spectral density as a function of frequency at the time marked by the vertical dotted line in Panel (a). (c) The electron phase space distribution. In all three panels, ω_{lb} and ω_{rb} are the left and right boundaries marking locations of full width half maximum of $\log_{10}(P_B)$ in Panel (b), and ω_p is the frequency of peaking wave intensity.

to the width of the resonant island, which is $\propto \omega_{tr}/k$ if measured in terms of v_{\parallel} . Therefore, a larger wave amplitude leads to a larger δp , and correspondingly a deeper amplitude modulation, if other parameters are fixed. This crude argument suggests that the increasing wave amplitude might contribute to the deeper amplitude modulation at $z/d_e = 80$ than at $z/d_e = 20$ in Figure 9. Of course, a more quantitative calculation is needed to confirm this argument.

Fourth, although the subpacket period T is estimated to be on the same order as ω_{tr}^{-1} , we may provide a refined estimate of T by taking into account that the resonant electrons move oppositely to the wave. Suppose the observation of the waveform and subpackets is made at a location z_0 , where the wave amplitude maximizes at time t_0 due to momentum exchange with electrons. The same group of phase-trapped electrons would cause another wave amplitude maximum after T_{tr} , which is $2\pi/\omega_{tr}$, at $z_0 + \Delta z$ with $\Delta z = v_r T_{tr}$. This new maximum will propagate to z_0 after a duration of $\Delta z/v_g$. Correspondingly, for an observer at z_0 , the time difference T between two maximum is about

$$T \sim \left(1 - \frac{v_r}{v_g}\right) T_{tr}. \quad (27)$$

Noting $v_r/v_g < 0$, $T/T_{tr} > 1$. For typical cases with $\mu \gg 1$, $v_r/v_g = -(2\omega/\Omega_e)^{-1}$. Therefore, $T \sim 3T_{tr}$ if $\omega/\Omega_e = 0.3$, or $2T_{tr}$ if $\omega/\Omega_e = 0.5$. For the waveform shown in $z/d_e = 80$, we may take $\Omega_e \approx \Omega_{e0}$, $\delta B/B_0 \sim 10^{-2}$, and therefore, $\omega_{tr}/\Omega_{e0} \sim 0.1$ with $\mu \sim 10$, $v_{\perp}/c \sim 0.3$, $\omega/\Omega_{e0} \sim 0.3$. This leads to $T_{tr} \sim 60$, and $T \sim 180$. The period roughly agrees with the period of subpacket at $z/d_e = 80$ shown in Figure 9f.

In summary, we conclude here that the conservation of momentum and energy between phase-trapped electrons and chorus waves is responsible for both the formation and the dynamic evolution of chorus subpackets. A quantitative description of subpackets should take into account the conservation laws and dynamics of phase-trapped electrons.

7.2. Instantaneous Bandwidth of Chorus Elements

Chorus waves are narrowband emissions, and the instantaneous bandwidth should be on the order of ω_{tr} due to nonlinear wave particle interactions, as illustrated in Figure 10. We use the wave spectrogram at $z = 0$ as an example (Figure 10a). To estimate the bandwidth, we plot the wave power spectral density P_B as a function of frequency at $t\Omega_{e0} = 2537$, as indicated by the vertical dashed line in Figure 10a. This particular time is chosen simply because there is a saved distribution of electrons. In Figure 10b, we estimate the bandwidth $\Delta\omega$ by the full width at half maximum of $\log_{10}(P_B)$. The left and right boundaries are denoted as $\omega_{lb} \approx 0.3\Omega_{e0}$ and $\omega_{rb} \approx 0.4\Omega_{e0}$; therefore, $\Delta\omega \approx 0.1\Omega_{e0}$. From Figure 10c, the two frequencies ω_{lb} and ω_{rb} roughly correspond to the resonant frequencies at the lower and upper boundaries of the resonant island. Since the width of the resonant island is $\mathcal{O}(\omega_{tr}/k)$ measured by v_{\parallel} , the difference between ω_{lb} and ω_{rb} or the instantaneous bandwidth of chorus is $\mathcal{O}(\omega_{tr})$. A more accurate estimate, of course, needs to take into account the value of R ; for example, if $R = 0$, the resonant island width is $4\omega_{tr}/k$. In case of Figure 5, $R \approx 0.5$;

therefore, $\Delta v_{\parallel} \approx 2\omega_r/k$. From Equation 13 and $\delta B/B_0 \approx 2 \times 10^{-3}$ at $z = 0$, we may estimate $\omega_r/\Omega_{e0} \approx 0.045$. Neglecting change of k , the resonant island width indicates that the bandwidth of chorus should be $0.09\Omega_{e0}$, consistent with the estimate by $|\omega_b - \omega_r|$.

We may use typical parameters in the magnetosphere to estimate the order of instantaneous bandwidth of chorus elements. We choose $\omega/\Omega_{e0} = 0.3$ as a representative frequency. Outside the plasmopause, we may take $\mu \sim 10$, and therefore $v_r \approx 0.2c$. With $v_{\perp} \sim 0.5c$, which corresponds to $\alpha \approx 70^\circ$, we arrive at $\omega_r/\Omega_{e0} \approx (\delta B/B_0)^{1/2}$ from Equation 13. At $L = 5$, $B_0 \approx 0.0024$ G, and $\Omega_{e0} \approx 42240$ rad/s. For the typical amplitude $\delta B/B_0 \sim 10^{-3}$, the bandwidth is on the order of 1335 rad/s or 212 Hz. This roughly agrees with observation that chorus elements typically have a bandwidth of a few hundred Hz.

Note that the bandwidth of chorus has a dependence on wave amplitude as $\delta B^{1/2}$. Correspondingly, stronger (weaker) elements tend to have larger (smaller) instantaneous bandwidth.

8. Summary

In this work, we presented a theory-based phenomenological model of chorus, the TaRA model, based on analysis of effective wave growth rate and electron phase space dynamics from a PIC simulation with the DAWN code. The TaRA model shares the same principle with many previous models in that nonlinear wave particle interactions phase organizes energetic electrons, and these phase-correlated electrons generate new coherent emissions. The difference among various models is on how the principle is applied to explain chirping and other properties of chorus in details. Our results could be summarized as follows:

1. The effective wave growth rate γ_{eff} is much larger in the upstream than in the downstream. This, combined with electron phase space dynamics analysis, demonstrates that the upstream region is mainly for generation of new emissions and wave amplification, while the downstream is mainly for phase-organizing resonant electrons by nonlinear wave particle interactions. The fact that $\gamma_{\text{eff}} \gg \gamma_L$ at wave excitation ensures the generation of narrowband emissions by phase-correlated electrons.
2. The TaRA model explains chirping of chorus by selective amplification of new emissions that satisfy the phase-locking condition with phase-correlated electrons released from the previously generated part of the packet. The phase-locking condition allows the longest possible resonant interaction and maximizes possible wave power transfer. At the release point, this condition leads to that chorus frequency chirping rate is determined by the background magnetic field inhomogeneity for the rising-tone chorus analyzed in this study. This chirping rate has the same form as the one given by Helliwell (1967).
3. The nonlinear wave particle interaction mainly occurs in the downstream. Correspondingly, the relation between frequency chirping rate and wave amplitude originally proposed by Vomvouridis et al. (1982) is also valid near the equator. The validity of this relation could be regarded as a proof of the important role played by nonlinear wave particle interactions in generation of chorus.
4. The TaRA model, therefore, unifies two different ways of estimating chorus chirping rate from Helliwell (1967) and Vomvouridis et al. (1982), and suggests that the difference between the two chirping rates could be explained by that they are derived at different stages of chorus generation. Correspondingly, this model explains why both chirping rates have been shown to agree very well with observations and simulations in previous studies.
5. Subpackets of chorus are explained by the conservation of momentum and energy between wave fields and phase-trapped electrons as in Tao et al. (2017a). This suggests that subpacket period and the number of subpackets for a given element are not fixed, but have a weak dependence on wave amplitude, exhibiting dynamic evolution as waves propagate from upstream to downstream.
6. The bandwidth of chorus is on the order of ω_r , which suggests that stronger elements tend to have larger bandwidth than weaker elements.

Our model is based on a PIC simulation for rising-tone chorus with a dipole-type background magnetic field. By properly taking into account different background plasma parameters and resonance conditions, it is potentially possible to explain various chirping phenomena previously reported with the same principle, including chirping of chorus in a uniform field, falling tone chorus, and chirping of electromagnetic ion cyclotron waves in the magnetosphere. The quantitative results obtained in the study should also be helpful

to understand different properties of chorus observed at Earth, Saturn (Hospodarsky et al., 2008) and Jupiter (Menietti et al., 2008). Finally, we emphasize that the purpose of the phenomenological TaRA model is mainly to elucidate how and where chirping occurs. A more quantitative analysis could be based on the theoretical framework of Zonca et al. (2017).

Data Availability Statement

Code and input files used for generating the data used in this study can be found at <https://doi.org/10.5281/zenodo.4774932>.

Acknowledgments

This work was supported by NSFC grants (41631071, 11235009 and 42174182), the Strategic Priority Program of the Chinese Academy of Sciences (No. XDB41000000), the Fundamental Research Funds for the Central Universities, EURATOM research and training programme 2014-2018 and 2019-2020 under grant agreement No. 633053. The views and opinions expressed herein do not necessarily reflect those of the European Commission. Xin Tao would like to dedicate this paper with gratitude and respect to the memory of Prof. Richard M. Thorne.

References

- Artemyev, A. V., Neishtadt, A. I., & Vasiliev, A. A. (2020). Mapping for nonlinear electron interaction with whistler-mode waves. *Physics of Plasmas*, 27(4), 042902. <https://doi.org/10.1063/1.5144477>
- Burtis, W. J., & Helliwell, R. A. (1976). Magnetospheric chorus: Occurrence patterns and normalized frequency. *Planetary and Space Science*, 24(11), 1007–1024. [https://doi.org/10.1016/0032-0633\(76\)90119-7](https://doi.org/10.1016/0032-0633(76)90119-7)
- Chen, L., & Zonca, F. (2016). Physics of Alfvén waves and energetic particles in burning plasmas. *Reviews of Modern Physics*, 88, 015008. <https://doi.org/10.1103/RevModPhys.88.015008>
- Cully, C. M., Angelopoulos, V., Auster, U., Bonnell, J., & Le Contel, O. (2011). Observational evidence of the generation mechanism for rising-tone chorus. *Geophysical Research Letters*, 38, L01106. <https://doi.org/10.1029/2010GL045793>
- Demekhov, A. G. (2011). Generation of VLF emissions with the increasing and decreasing frequency in the magnetospheric cyclotron maser in the backward wave oscillator regime. *Radiophysics and Quantum Electronics*, 53(11), 609–622. <https://doi.org/10.1007/s11141-011-9256-x>
- Demekhov, A. G., & Trakhtengerts, V. Y. (2008). Dynamics of the magnetospheric cyclotron ELF/VLF maser in the backward-wave-oscillator regime. II. The influence of the magnetic-field inhomogeneity. *Radiophysics and Quantum Electronics*, 51(11), 880–889. <https://doi.org/10.1007/s11141-009-9093-3>
- Giannessi, L., Musumeci, P., & Spampinati, S. (2005). Nonlinear pulse evolution in seeded free-electron laser amplifiers and in free-electron laser cascades. *Journal of Applied Physics*, 98(4), 043110. <https://doi.org/10.1063/1.2010624>
- Hanzelka, M., Santolik, O., Omura, Y., Kolmašová, I., & Kletzing, C. A. (2020). A model of the subpacket structure of rising tone chorus emissions. *Journal of Geophysical Research: Space Physics*, 125(8), e28094. <https://doi.org/10.1029/2020JA028094>
- Heidbrink, W. W. (1995). Beam-driven chirping instability in DIII-D. *Plasma Physics and Controlled Fusion*, 37(9), 937–949. <https://doi.org/10.1088/0741-3335/37/9/002>
- Helliwell, R. A. (1967). A theory of discrete VLF emissions from the magnetosphere. *Journal of Geophysical Research*, 72(19), 4773–4790. <https://doi.org/10.1029/jz072i019p04773>
- Hikishima, M., Yagitani, S., Omura, Y., & Nagano, I. (2009). Full particle simulation of whistler-mode rising chorus emissions in the magnetosphere. *Journal of Geophysical Research*, 114, A01203. <https://doi.org/10.1029/2008JA013625>
- Horne, R. B., Thorne, R. M., Shprits, Y. Y., Meredith, N. P., Glauert, S. A., Smith, A. J., et al. (2005). Wave acceleration of electrons in the Van Allen radiation belts. *Nature*, 437, 227–230. <https://doi.org/10.1038/nature03939>
- Hospodarsky, G. B., Averkamp, T. F., Kurth, W. S., Gurnett, D. A., Menietti, J. D., Santoik, O., & Dougherty, M. K. (2008). Observations of chorus at Saturn using the Cassini Radio and plasma wave science instrument. *Journal of Geophysical Research*, 113, A12206. <https://doi.org/10.1029/2008JA013237>
- Hu, G., & Krommes, J. A. (1994). Generalized weighting scheme for δf particle-simulation method. *Physics of Plasmas*, 1(4), 863–874. <https://doi.org/10.1063/1.870745>
- Inan, U. S., Bell, T. F., & Helliwell, R. A. (1978). Nonlinear pitch angle scattering of energetic electrons by coherent VLF waves in the magnetosphere. *Journal of Geophysical Research*, 83(A7), 3235–3253. <https://doi.org/10.1029/ja083ia07p03235>
- Kasahara, S., Miyoshi, Y., Yokota, S., Mitani, T., Kasahara, Y., Matsuda, S., et al. (2018). Pulsating aurora from electron scattering by chorus waves. *Nature*, 554(7692), 337–340. <https://doi.org/10.1038/nature25505>
- Katoh, Y., & Omura, Y. (2007). Computer simulation of chorus wave generation in the Earth's inner magnetosphere. *Geophysical Research Letters*, 34, L03102. <https://doi.org/10.1029/2006GL028594>
- Katoh, Y., & Omura, Y. (2011). Amplitude dependence of frequency sweep rates of whistler mode chorus emissions. *Journal of Geophysical Research*, 116, A07201. <https://doi.org/10.1029/2011JA016496>
- Katoh, Y., & Omura, Y. (2013). Effect of the background magnetic field inhomogeneity on generation processes of whistler-mode chorus and broadband hiss-like emissions. *Journal of Geophysical Research: Atmospheres*, 118, 4189–4198. <https://doi.org/10.1002/jgra.50395>
- Ke, Y., Gao, X., Lu, Q., Wang, X., & Wang, S. (2017). Generation of rising-tone chorus in a two-dimensional mirror field by using the general curvilinear PIC code. *Journal of Geophysical Research: Space Physics*, 122, 8154–8165. <https://doi.org/10.1002/2017JA024178>
- Menietti, J. D., Horne, R. B., Gurnett, D. A., Hospodarsky, G. B., Piker, C. W., & Groene, J. B. (2008). A survey of Galileo plasma wave instrument observations of Jovian whistler-mode chorus. *Annales Geophysicae*, 26, 1819–1828. <https://doi.org/10.5194/angeo-26-1819-2008>
- Mourenas, D., Artemyev, A. V., Agapitov, O. V., Krasnoselskikh, V., & Mozer, F. S. (2015). Very oblique whistler generation by low-energy electron streams. *Journal of Geophysical Research: Space Physics*, 120(5), 3665–3683. <https://doi.org/10.1002/2015JA021135>
- Mourenas, D., Zhang, X.-J., Artemyev, A. V., Angelopoulos, V., Thorne, R. M., Bortnik, J., et al. (2018). Electron nonlinear resonant interaction with short and intense parallel chorus wave packets. *Journal of Geophysical Research: Space Physics*, 123(6), 4979–4999. <https://doi.org/10.1029/2018JA025417>
- Nishimura, Y., Bortnik, J., Li, W., Thorne, R. M., Lyons, L. R., Angelopoulos, V., et al. (2010). Identifying the driver of pulsating aurora. *Science*, 330(6000), 81–84. <https://doi.org/10.1126/science.1193186>
- Nunn, D. (1974). A self-consistent theory of triggered VLF emissions. *Planetary and Space Science*, 22(3), 349–378. [https://doi.org/10.1016/0032-0633\(74\)90070-1](https://doi.org/10.1016/0032-0633(74)90070-1)
- Nunn, D. (1986). A nonlinear theory of sideband stability in ducted whistler mode waves. *Planetary and Space Science*, 34(5), 429–451. [https://doi.org/10.1016/0032-0633\(86\)90032-2](https://doi.org/10.1016/0032-0633(86)90032-2)

- Nunn, D. (1990). The numerical simulation of VLF nonlinear wave-particle interactions in collision-free plasmas using the Vlasov hybrid simulation technique. *Computer Physics Communications*, 60, 1–25. [https://doi.org/10.1016/0010-4655\(90\)90074-B](https://doi.org/10.1016/0010-4655(90)90074-B)
- Nunn, D., Omura, Y., Matsumoto, H., Nagano, I., & Yagitani, S. (1997). The numerical simulation of VLF chorus and discrete emissions observed on the Geotail satellite using a Vlasov code. *Journal of Geophysical Research*, 102(A12), 27083–27097. <https://doi.org/10.1029/97ja02518>
- Nunn, D., Zhang, X.-J., Mourenas, D., & Artemyev, A. V. (2021). Generation of realistic short chorus wave packets. *Geophysical Research Letters*, 48, e2020GL092178. <https://doi.org/10.1029/2020GL092178>
- Omura, Y. (2021). Nonlinear wave growth theory of whistler-mode chorus and hiss emissions in the magnetosphere. *Earth, Planets, and Space*, 73(1), 95. <https://doi.org/10.1186/s40623-021-01380-w>
- Omura, Y., Katoh, Y., & Summers, D. (2008). Theory and simulation of the generation of whistler-mode chorus. *Journal of Geophysical Research*, 113, A04223. <https://doi.org/10.1029/2007JA012622>
- Omura, Y., & Nunn, D. (2011). Triggering process of whistler mode chorus emissions in the magnetosphere. *Journal of Geophysical Research*, 116, A05205. <https://doi.org/10.1029/2010JA016280>
- O'Neil, T. (1965). Collisionless damping of nonlinear plasma oscillations. *Physics of Fluids*, 8, 2255–2262. <https://doi.org/10.1063/1.1761193>
- Parker, S. E., & Lee, W. W. (1993). A fully nonlinear characteristic method for gyrokinetic simulation. *Physics of Fluids B*, 5(1), 77–86. <https://doi.org/10.1063/1.860870>
- Pickett, J. S., Grison, B., Omura, Y., Engebretson, M. J., Dandouras, I., Masson, A., et al. (2010). Cluster observations of EMIC triggered emissions in association with Pc1 waves near Earth's plasmapause. *Geophysical Research Letters*, 37, L09104. <https://doi.org/10.1029/2010GL042648>
- Reeves, G. D., Spence, H. E., Henderson, M. G., Morley, S. K., Friedel, R. H. W., Funsten, H. O., et al. (2013). Electron acceleration in the heart of the Van Allen radiation belts. *Science*, 341(6149), 991–994. <https://doi.org/10.1126/science.1237743>
- Sagdeev, R. Z., Shapiro, V. D., & Shevchenko, V. I. (1985). Mechanism of triggered emission in the magnetospheric plasma. *Zhurnal Eksperimental'noi i Teoreticheskoi Fiziki*, 89, 22–33.
- Santolik, O., Gurnett, D. A., Pickett, J. S., Parrot, M., & Cornilleau-Wehrlin, N. (2004). A microscopic and nanoscopic view of storm-time chorus on 31 March 2001. *Geophysical Research Letters*, 31, L02801. <https://doi.org/10.1029/2003GL018757>
- Santolik, O., Kletzing, C. A., Kurth, W. S., Hospodarsky, G. B., & Bounds, S. R. (2014). Fine structure of large-amplitude chorus wave packets. *Geophysical Research Letters*, 41, 293–299. <https://doi.org/10.1002/2013GL058889>
- Shklyar, D. (2011). On the nature of particle energization via resonant wave-particle interaction in the inhomogeneous magnetospheric plasma. *Annales Geophysicae*, 29(6), 1179–1188. <https://doi.org/10.5194/angeo-29-1179-2011>
- Shklyar, D., & Matsumoto, H. (2009). Oblique whistler-mode waves in the inhomogeneous magnetospheric plasma: Resonant interactions with energetic charged particles. *Surveys in Geophysics*, 30(2), 55–104. <https://doi.org/10.1007/s10712-009-9061-7>
- Shoji, M., & Omura, Y. (2013). Triggering process of electromagnetic ion cyclotron rising tone emissions in the inner magnetosphere. *Journal of Geophysical Research: Space Physics*, 118(9), 5553–5561. <https://doi.org/10.1002/jgra.50523>
- Soto-Chavez, A. R., Bhattacharjee, A., & Ng, C. S. (2012). Chorus wave amplification: A free electron laser in the Earth's magnetosphere. *Physics of Plasmas*, 19(1), 010701. <https://doi.org/10.1063/1.3676157>
- Stix, T. H. (1992). *Waves in plasmas*. American Institute of Physics.
- Sudan, R. N., & Ott, E. (1971). Theory of triggered VLF emissions. *Journal of Geophysical Research*, 76(19), 4463–4476. <https://doi.org/10.1029/JA076i019p04463>
- Tao, X. (2014). A numerical study of chorus generation and the related variation of wave intensity using the DAWN code. *Journal of Geophysical Research: Space Physics*, 119, 3362–3372. <https://doi.org/10.1002/2014JA019820>
- Tao, X., Li, W., Bortnik, J., Thorne, R. M., & Angelopoulos, V. (2012). Comparison between theory and observation of the frequency sweep rates of equatorial rising tone chorus. *Geophysical Research Letters*, 39, L08106. <https://doi.org/10.1029/2012GL051413>
- Tao, X., Lu, Q., Wang, S., & Dai, L. (2014). Effects of magnetic field configuration on the day-night asymmetry of chorus occurrence rate: A numerical study. *Geophysical Research Letters*, 41, 6577–6582. <https://doi.org/10.1002/2014GL061493>
- Tao, X., Zonca, F., & Chen, L. (2017a). Identify the nonlinear wave-particle interaction regime in rising tone chorus generation. *Geophysical Research Letters*, 44(8), 3441–3446. <https://doi.org/10.1002/2017GL072624>
- Tao, X., Zonca, F., & Chen, L. (2017b). Investigations of the electron phase space dynamics in triggered whistler wave emissions using low noise δf method. *Plasma Physics and Controlled Fusion*, 59(9), 094001. <https://doi.org/10.1088/1361-6587/aa759a>
- Tao, X., Zonca, F., Chen, L., & Wu, Y. (2020). Theoretical and numerical studies of chorus waves: A review. *Science China Earth Sciences*, 63, 78–92. <https://doi.org/10.1007/s11430-019-9384-6>
- Thorne, R. M., Li, W., Ni, B., Ma, Q., Bortnik, J., Chen, L., et al. (2013). Rapid local acceleration of relativistic radiation-belt electrons by magnetospheric chorus. *Nature*, 504, 411–414. <https://doi.org/10.1038/nature12889>
- Thorne, R. M., Ni, B., Tao, X., Horne, R. B., & Meredith, N. P. (2010). Scattering by chorus waves as the dominant cause of diffuse auroral precipitation. *Nature*, 467, 943–946. <https://doi.org/10.1038/nature09467>
- Titova, E. E., Kozelov, B. V., Jiriček, F., Smilauer, J., Demekhov, A. G., & Trakhtengerts, V. Y. (2003). Verification of the backward wave oscillator model of VLF chorus generation using data from MAGION 5 satellite. *Annales Geophysicae*, 21, 1073–1081. <https://doi.org/10.5194/angeo-21-1073-2003>
- Trakhtengerts, V. Y. (1995). Magnetosphere cyclotron maser: Backward wave oscillator generation regime. *Journal of Geophysical Research*, 100(A9), 17205–17210. <https://doi.org/10.1029/95ja00843>
- Tsurutani, B. T., Chen, R., Gao, X., Lu, Q., Pickett, J. S., Lakhina, G. S., et al. (2020). Lower-band “monochromatic” chorus riser subelement/wave packet observations. *Journal of Geophysical Research: Space Physics*, 125, e2020JA028090. <https://doi.org/10.1029/2020JA028090>
- Tsurutani, B. T., & Smith, E. J. (1974). Postmidnight chorus: A substorm phenomenon. *Journal of Geophysical Research*, 79(1), 118–127. <https://doi.org/10.1029/ja079i001p0118>
- Vomvoridis, J. L., Crystal, T. L., & Denavit, J. (1982). Theory and computer simulations of magnetospheric very low frequency emissions. *Journal of Geophysical Research*, 87(A3), 1473–1489. <https://doi.org/10.1029/JA087iA03p01473>
- Wu, Y., Tao, X., Zonca, F., Chen, L., & Wang, S. (2020). Controlling the chirping of chorus waves via magnetic field inhomogeneity. *Geophysical Research Letters*, 47(10), e2020GL087791. <https://doi.org/10.1029/2020GL087791>
- Zhang, X.-J., Mourenas, D., Artemyev, A. V., Angelopoulos, V., Bortnik, J., Thorne, R. M., et al. (2019). Nonlinear electron interaction with intense chorus waves: Statistics of occurrence rates. *Geophysical Research Letters*, 46(13), 7182–7190. <https://doi.org/10.1029/2019GL083833>
- Zhang, X.-J., Thorne, R., Artemyev, A., Mourenas, D., Angelopoulos, V., Bortnik, J., et al. (2018). Properties of intense field-aligned lower-band chorus waves: Implications for nonlinear wave-particle interactions. *Journal of Geophysical Research: Space Physics*, 123(7), 5379–5393. <https://doi.org/10.1029/2018JA025390>

- Zonca, F., Chen, L., Briguglio, S., Fogaccia, G., Milovanov, A. V., Qiu, Z., et al. (2015). Energetic particles and multi-scale dynamics in fusion plasmas. *Plasma Physics and Controlled Fusion*, 57(1), 014024. <https://doi.org/10.1088/0741-3335/57/1/014024>
- Zonca, F., Chen, L., Briguglio, S., Fogaccia, G., Vlad, G., & Wang, X. (2015). Nonlinear dynamics of phase space zonal structures and energetic particle physics in fusion plasmas. *New Journal of Physics*, 17(1), 031052. <https://doi.org/10.1088/1367-2630/17/1/013052>
- Zonca, F., Tao, X., & Chen, L. (2017). Nonlinear wave-particle dynamics in chorus excitation. In *44th EPS conference on plasma physics* (Vol. 41F). Belfast, Northern Ireland.